# Applying hybrid methods to reduce nonphysical cycles in the flux field

Christine Marie Øvrebø Haugland

**Abstract**

In this thesis we present the theoretical background for the two-point flux-approximation method; (TPFA), mimetic discretisation methods, and the multipoint flux approximation method; (MPFA). Theoretical arguments concerning monotonicity and the fact that loss of monotonicity may lead to oscillations and nonphysical cycles in the flux field are also discussed. TPFA is only consistent for **K**-orthogonal grids. Multipoint flux approximation methods and mimetic discretisation methods are consistent, even for grids that are not **K**-orthogonal, but sometimes they lead to solutions containing cycles in the flux field. These cycles may cause problems for some transport solvers and diminish the efficiency of others, and to try to cure this problem, we present two hybrid methods. The first is a hybrid mimetic method applying TPFA in the vertical direction and mimetic discretisation in the plane. The second hybrid method is the hybrid MPFA method applying TPFA in the vertical direction and MPFA in the plane. We present results comparing the accuracy of the methods and the number of cycles obtained by the different methods. The results obtained shows that the hybrid methods are more accurate than TPFA, and for specific cases they have less cycles than the original full methods.

## Sammendrag

I denne oppgaven presenteres den teoretiske bakgrunnen for topunkts fluksapproksimasjon; (TPFA), mimetiske diskretiseringsmetoder og flerpunkts fluksapproksimasjon; (MPFA). Teoretiske argumenter rundt monotoni og det faktum at tap av monotoni kan føre til svingninger og sykler i fluksfeltet, som ikke er fysisk mulige, blir også diskutert. Topunkts fluksapproksimasjon er bare konsistent for gitre som er K-ortogonale. Flerpunkts fluksapproksimasjoner og mimetiske diskretiseringsmetoder er konsistente, selv for gitre som ikke er K-ortogonale, men de fører noen ganger til løsninger som inneholder sykler i fluksfeltet. Syklene kan forårsake problemer for noen tranportløsere og minke effektiviteten av andre, i forsøk på å finne en løsning på dette problemet vil vi presenterer to hybride metoder. Den første er en hybrid mimetisk metode som bruker TPFA i vertikal retning og mimetisk diskretisering i planet. Den andre hybride metoden er hybrid MPFA som bruker TPFA i vertikal retning og MPFA i planet. Vi presenterer resultater der vi sammenligner nøyaktigheten av metodene og antall sykler som fremkommer ved bruk av de ulike metodene. Resultatene viser at de hybride metodene er mer eksakte enn TPFA og ved noen tilfeller har de færre sykler enn mimetiske metoder og MPFA.

# Preface

This master thesis is submitted as the final work of my masters degree in Industrial Mathematics at the Department of Mathematical Sciences at the Norwegian University of Science and Technology, NTNU.

I would like to thank my supervisors at SINTEF ICT, at the Department of Applied Mathematics. Thank you Stein Krogstad for explaining parts of the theory to me, helping me with my programming and providing me with useful test examples. I would also like to thank you for helping me to best present my results and commenting on my thesis. I would like to thank Knut-Andreas Lie for answering many of my questions and helping me with my understanding. In addition I would like to thank you for reading and giving me comments on my paper. Furthermore I would thank my supervisor at NTNU, Helge Holden, for introducing me to SINTEF and giving me feedback on my thesis. Last semester I wrote my specialisation project which touched upon the same topic as this master thesis. Halvor Møll Nilsen was my supervisor on this project, in addition to Knut-Andreas Lie and Helge Holden. I want to thank Halvor for helping me with my project where I learned a lot that I have also used in my master thesis.

I would also thank my friends and family for always being there for me, especially my father, Sven Haugland, who in addition have read and commented on my thesis.

# Contents

# 7  Bibliography                                                    65

# Chapter 1

# Introduction

Reservoir simulation is an important area within oil reservoir management. The simulations can provide a better understanding of the flow patterns in the reservoir, and simulations can be helpful in determining the placement of wells in order to obtain the most optimal oil and gas recovery. Getting an accurate prediction of the flow in a reservoir is difficult because numerous factors may impact the flow. It is not possible to model all rock properties in the entire reservoir accurately, and even if it was, it would result in too much information to process. Hence, we have to make certain approximations in which the rock properties are constant within one grid block.

Furthermore, we cannot include all of the properties of the reservoir at the same time. The domain that represent the reservoir must be divided into grid blocks. Results are calculated for all the grid blocks in the reservoir and then added together. It is possible to develop geological models down to a meter scale [1], but such models result in too many grid blocks making the simulation too computationally costly. Instead we have to make the grid blocks larger and upscale the geophysical parameters.

Developing numerical methods to approximate complex physical properties is an important part of applied mathematics, and research has been concerned with flow modelling in porous media. This thesis will focus on oil flowing through a porous media; the reservoir. However, the methods presented may also be used in simulations of other fluids. Several different numerical discretisation methods exist, and selecting the best one depends on the specific problem to be solved. The most common discretisation method used in reservoir simulation is the two-point flux-approximation method (TPFA, see e.g., [1, 2, 3]). TPFA result in a cell-centred system. This method is computationally efficient, but is only consistent for $\mathbf{K}$-orthogonal grids. Generally, the grid blocks used in reservoir simulation are larger in the $xy$-plane than in the $z$-direction. In addition, the permeability in the $z$-direction is usually small compared to the permeability in the plane, therefore most of the flow is along the layers. Consequently it is likely to believe that most of the errors by using TPFA occur in the plane.

In recent years research concerning the monotonicity of discretisation methods shows that TPFA is always monotone. Loss of monotonicity may be caused by oscillations in the pressure and an effect of this may be that artificial gas is liberated which leads to a

strongly diverging solution [4]. When a method is not monotone, nonphysical cycles in the flux field may occur. Cycles in the flux field may lead to longer computational time.

Other discretisation methods well suited for the oil industry exist as well. One of these methods is the group of mimetic methods, [5], which are defined in terms of a transmissibility matrix, **T**, which is an inverse inner product. The mimetic methods are designed in such a way that they are exact for linear pressure fields, and hence are consistent. However, the mimetic methods tend to be non-monotone for grids where the grid blocks are skew, and these methods require more computation than TPFA. The mimetic methods result in an edge-centred system of unknown pressures.

Another group of methods which has received much attention in resent research is the multipoint flux approximation methods; (MPFA, [3, 6]). MPFA-methods are consistent for grids which are not **K**-orthogonal, but these methods are not always monotone and they require more computation than TPFA. As TPFA, MPFA lead to a cell-centred system.

This thesis will present the theoretical background for TPFA, mimetic methods and MPFA. Regarding the mimetic methods, we will focus on an inner-product called `ip_simple` in MRST, while we for the MPFA will present the theory for the MPFA-O method and a local-flux mimetic formulation of MPFA-O, [7, 8].

*The goal of this thesis is to develop methods using TPFA in the vertical direction and a consistent method in the plane. The motivation for doing this is to obtain methods which are more consistent than TPFA and results in fewer cycles in the flux field compared to using the consistent methods in the entire domain.*

We seek to explore the accuracy of a method using TPFA in the $z$-direction and a more consistent method in the $xy$-plane, and if the number of cycles decreases compared to the consistent method. We call these new methods hybrid methods. We will present two hybrid methods. The first builds on TPFA and the mimetic method using `ip_simple` as inner product. The second builds on TPFA and the local-flux mimetic formulation of the MPFA-O method, see e.g., [9].

The two hybrid methods are implemented in MATLAB by using Matlab Reservoir Simulation Toolbox; (MRST). MRST, is an open-source MATLAB toolkit developed by SINTEF [10]. Using MRST, we have performed simulations on different types of grids and compared the results of the two hybrid methods to TPFA and their respective consistent methods. The hybrid methods and some of the test examples can be found in the MRST add-on module `HybridMethods`.

# Chapter 2

# Discretisation models

## 2.1 Introduction to reservoir simulation

Reservoir simulation is an important part of oil-reservoir management. Simulations are used to help the oil companies estimate production characteristics, calibrate reservoir parameters, visualise the flow patterns in the reservoir, etc [1]. The challenges in predicting reservoir behaviour depend both on obtaining the most accurate geological parameters, and using these parameters in numerical calculations. In this thesis we will concentrate on solving for the pressure in the reservoir. Oil reservoirs are characterised by complex geometry and rapid changes in rock properties. This requires numerical methods which can be used on complex grids, and the methods need to handle discontinuities in the parameters.

### 2.1.1 Rock properties

The rock properties are the properties of the rock in the reservoir affecting the flow pattern of the oil. This includes the geophysical properties of the rock, for example permeability and porosity, and the dimensional properties.

The permeability **K** is a property of the rock, i.e., it gives a measure of the rock's ability to transmit fluids. The permeability is a property of the reservoir and not the oil in the reservoir. **K** is a tensor of size $d \times d$ where $d$ is the spatial dimension. The permeability tensor is symmetric and positive definite, and the elements in the matrix can be written as:

$$\mathbf{K} = \begin{bmatrix} k_{ii} & k_{ij} & k_{ik} \\ k_{ji} & k_{jj} & k_{jk} \\ k_{ki} & k_{kj} & k_{kk} \end{bmatrix}. \tag{2.1}$$

The SI unit for permeability is $m^2$, but it is more common to use the unit Darcy, 1D

$\approx 0.987 \cdot 10^{-12} m^2$. In oil reservoirs, a permeability of 1D is a relatively high permeability. There are many different rock formations with different permeabilities in one oil field, and hence, the permeability may vary over several orders of magnitude. It is not unusual to have variations in the range of 1 mD to 10 D [1]. If the permeability is homogeneous, it means that the permeability is the same for all the grid blocks in the reservoir, while heterogeneous permeability means that all the grid blocks in the reservoir have strongly varying permeability. It is also common to talk about isotropic and anisotropic permeability. Isotropic permeability means that the permeability is the same in all directions while anisotropic permeability means that it is not the same in all directions.

The porosity, $\phi$, is also a property of the rock, and it is the void fraction of the volume of the rock, hence $0 \le \phi < 1$. The rock is compressible, and hence the porosity depends on the pressure. The rock compressibility is

$$c_r = \frac{1}{\phi} \frac{d\phi}{dp},$$ (2.2)

where $p$ is the pressure in the reservoir. For reservoirs in the North Sea, the value of $\phi$ is normally $0.1 - 0.3$ [1].

In this thesis we will only consider single-phase flow. However, when considering reservoir simulation, it is common to talk about multiphase flow. Therefore, we will briefly introduce a few properties that are being used when multiphase flow is considered.

In reservoir simulations we usually consider the void of the porous media to consist of three different phases. These phases are: aqueous ($w$), oleic ($o$) and gaseous ($g$). The fraction of the volume occupied by one phase is the saturation of that phase, ($s$).

$$\sum_{i=(o,g,w)} s_i = 1.$$ (2.3)

Each phase consists of one or more components. Here, a component is a hydrocarbon e.g., methane ethane, propane etc. And the sum of the mass fractions of each component in a phase should add up to 1, hence if $m_{ij}$ is the mass fraction of component $i$ in phase $j$ we have:

$$\sum_{i=1}^{N} m_{ig} = \sum_{i=1}^{N} m_{io} = \sum_{i=1}^{N} m_{iw} = 1,$$ (2.4)

where $N$ is the number of components, [1].

The different phases also have different pressures because of interfacial tensions. We therefore introduce the capillary pressure which is:

4

$$p_{cij} = p_i - p_j, \tag{2.5}$$

where $i, j = g, o, w$.

Oil reservoirs are characterized by complex geometry. The reservoir cannot be modelled exactly, and we therefore need to divide it into grid blocks where the physical parameters within one grid block are consistent. The technology today makes it possible to model the reservoir by grid blocks down to the meter scale, and these models consist of multi-million cells. Even very advanced computers will face problems in handling such a high number of cells. Therefore we need to upscale the geophysical parameters and use a coarse model with grid blocks which are ten to hundred times larger than the original grid blocks.

### 2.1.2   Mathematical model

The simplest mathematical model for an oil reservoir is the single-phase flow model. In this thesis it is assumed that we have one phase, i.e., only oil which we consider to be homogeneous, i.e., one can consider the phase as one component. The first equation which is used to model the flow through the reservoir is the continuity equation which states that mass is conserved [1],

$$\frac{\partial(\phi\rho)}{\partial t} + \nabla \cdot (\rho\vec{v}) = q. \tag{2.6}$$

Here $\phi$ is the porosity, $\rho$ is the density and $q$ is the source/sink term. This means that for a volume $\Omega$, the mass that is being produced by the source, $q$, in $\Omega$ equals the mass that stays in $\Omega$ plus the mass flowing out of $\Omega$.

The velocity, $\vec{v}$ in Equation (2.6) is given by Darcy's law:

$$\vec{v} = -\frac{\mathbf{K}}{\mu}(\nabla p + \rho g \nabla z), \tag{2.7}$$

where $\mathbf{K}$ is the permeability, $\mu$ the viscosity and $p$ is the pressure. The velocity $\vec{v}$ is very small, a typical value is approximately 1 Km per year [2].

If one assumes that the porosity is constant in time and if we have an incompressible fluid, i.e., the density is constant, Equation (2.6) becomes $\nabla \cdot \vec{v} = \frac{q}{\rho}$. Combining this with Equation (2.7) gives us the following:

$$\nabla \cdot \vec{v} = -\nabla \cdot \lambda \nabla u = \frac{q}{\rho}, \tag{2.8}$$

where $\lambda = \frac{K}{\mu}$ and is called the mobility, $u = (p + \rho g z)$ is the flow potential which is a function of the pressure. Equation 2.8 is an elliptic equation.

In this thesis we will consider finitely domains and we will not have any flow across the boundary. Hence, on the boundary $\partial \Omega$, we have $\vec{v} \cdot \vec{n} = 0$, $\vec{n}$ is the normal vector pointing out of $\partial \Omega$. When this is imposed on our domain we will have a system where no oil can enter or exit the reservoir.

### 2.1.3 Numerical methods

In order for the model to produce any output, for example, run a simulation of what happens in the reservoir, one need to solve a set of equations. We usually make an approximation of the flux, $\mathbf{f}$, through an interface $\gamma$:

$$\mathbf{f} = -\int_{\gamma} \frac{K}{\mu} \nabla u \cdot \vec{n} \, dv. \tag{2.9}$$

In discrete form one can write:

$$\mathbf{f}_i = \mathbf{T}_i (\mathbf{e}_i \mathbf{u}_i - \boldsymbol{\pi}_i), \quad \mathbf{e}_i = (1, ..., 1)^T, \tag{2.10}$$

where $\mathbf{u}_i$ is the pressure at the cell centre, $\boldsymbol{\pi}_i$ is the face potential and $\mathbf{T}_i$ is the transmissibility matrix for cell $i$. The transmissibility matrix will be discussed often throughout this thesis.

For numerical schemes which can be written in hybridised mixed form; by augmenting Equation (2.10) with continuity of flux and pressure across cell faces we, according to [5], get:

$$\begin{bmatrix} \mathbf{B} & \mathbf{C} & \mathbf{D} \\ \mathbf{C}^T & \mathbf{0} & \mathbf{0} \\ \mathbf{D}^T & \mathbf{0} & \mathbf{0} \end{bmatrix} \begin{bmatrix} \mathbf{f} \\ -\mathbf{u} \\ \boldsymbol{\pi} \end{bmatrix} = \begin{bmatrix} \mathbf{0} \\ \mathbf{q} \\ \mathbf{0} \end{bmatrix}, \tag{2.11}$$

where $\mathbf{B}$ is block-diagonal and the $i$'th block is $\mathbf{T}_i^{-1}$. The matrix $\mathbf{C}$ is also block-diagonal and the $i$'th block corresponds to cell $i$. The columns in $\mathbf{D}$ correspond to a unique face and it has unit entries corresponding to the index of the face in the cell-wise ordering. It has one entry for boundary faces and two entries for interior faces. If we consider a face that is connected to cell $i$ and cell $j$, but it is considered according to cell $i$, we call it a half face.

There are numerous different numerical schemes which can be used to discretise the equations and they all have their pros and cons. Some are fast, but may be inconsistent, while others are accurate, but very time-consuming. In this thesis, we will pay special attention to the numerical aspects of reservoir simulation. Equation (2.9) is a simple

version of the pressure equations and this has to be solved in order to run reservoir simulations.

## 2.2 Two-point flux approximation

The most common discretisation scheme used for reservoir simulation in the oil industry is the two-point flux-approximation; (TPFA) scheme. TPFA is a finite volume method, and finite volume methods are derived from conservation of physical quantities over cell volumes, for instance, mass. In this section we want to derive the two-point flux approximation, and the calculations in this section will follow [1]. Consider the following equation:

$$-\nabla \cdot \lambda \nabla u = \frac{q}{\rho}. \tag{2.12}$$



$$\Delta x_{i-1} \qquad \Delta x_i \qquad \Delta x_{i+1}$$

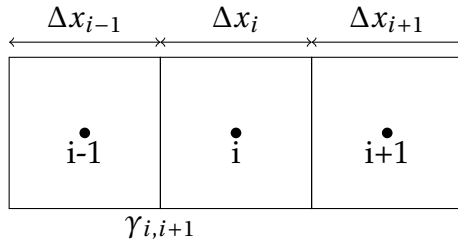i-1      i      i+1

$$\gamma_{i,i+1}$$

**Figure 2.1:** *Grid.*

Figure 2.1 shows a simple cell-centred grid. This grid can be used as an illustration to explain one dimensional horizontal flow. The cells are assigned indices, and these indices refer to the mid-point of each cell [2]. The interface, $\gamma_{i,i+1}$, is the common interface between cell $i$ and cell $i+1$, and we can say that this interface goes through the point $i+1/2$, but we do not know anything about it except that it is on the boundary between cell $i$ and cell $i+1$.

We want to approximate the flux, $\mathbf{f}_{i,i+1}$ between two cells, cell $i$ and cell $i+1$,

$$\mathbf{f}_{i,i+1} = -\int_{\gamma_{i,i+1}} (\frac{\mathbf{K}}{\mu} \nabla u) \cdot \vec{n} dv. \tag{2.13}$$

Two points are used, the mid-points of cell $i$ and $i+1$ and the potentials at these points are said to be $u_i$ and $u_{i+1}$. These potentials are cell averages. Assume that the gridlines are aligned with the principal coordinate axes and cell $i$ and $i+1$ are two cells with a common face, $\gamma_{i,i+1}$ which lies in the yz-plane. The flow is in the x-direction, it flows from cell $i$ to cell $i+1$. By using Taylor expansion one can find an expression for $\nabla u$:

**Proposition 2.2.1.** *For one-dimensional flow one can approximate $\nabla u$ by Taylor expansion leading to:*

$$\nabla u \approx \frac{2(u_{i+1} - u_i)}{\Delta x_{i+1} + \Delta x_i}. \tag{2.14}$$

7

*Proof.*

$$u_i = u_{i+1/2} - \frac{\Delta x_i}{2}\frac{\partial u_{i+1/2}}{\partial x} + O(\Delta x_i^2),$$

$$u_{i+1} = u_{i+1/2} + \frac{\Delta x_{i+1}}{2}\frac{\partial u_{i+1/2}}{\partial x} + O(\Delta x_{i+1}^2),$$

$$\frac{\partial u_{i+1/2}}{\partial x} \approx \frac{2(u_{i+1} - u_i)}{\Delta x_{i+1} + \Delta x_i}. \tag{2.15}$$

The dimension in the x-direction of cell $i$ is $\Delta x_i$. $\qquad\qquad\square$

Inserting Equation (2.14) into the expression for the flux gives the following equation:

$$\mathbf{f}_{i,i+1} = -\frac{2(u_{i+1} - u_i)}{\Delta x_{i+1} + \Delta x_i}\int_{\gamma_{i,i+1}} \frac{\mathbf{K}}{\mu}\cdot\vec{n}\,dv. \tag{2.16}$$

We let $\vec{\omega} = \mathbf{K}\vec{n}$, hence $\vec{\omega}_i = \mathbf{K}_i\vec{n}_i$ and $\vec{\omega}_{i+1} = \mathbf{K}_{i+1}\vec{n}_{i+1}$. The potential-difference used in Equation (2.15) is a good approximation if the line between $x_i$ and $x_{i+1/2}$ is parallel to $\vec{\omega}_i$ and the line between $x_{i+1/2}$ and $x_{i+1}$ is parallel to $\vec{\omega}_{i+1}$. When this is true, our grid is **K**-orthogonal, and hence, the following TPFA is only consistent for **K**-orthogonal grids [3].



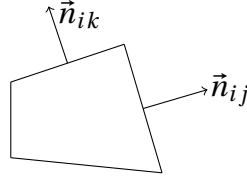**Figure 2.2:** *Cell with unit normal vectors.*

**Definition 2.2.1. K**-orthogonality
*A grid is **K**-orthogonal if, for all cells, the following is fulfilled:*

$$\vec{n}_{ij}\cdot\mathbf{K}\vec{n}_{ik} = 0, \qquad \forall\Omega_i \in \Omega, \qquad j \neq k,$$

$$\vec{n}_{ij}\cdot\vec{\omega}_{ik} = 0. \tag{2.17}$$

It is assumed that the mass is conserved and hence $\mathbf{f}_{i,i+1}$ must be constant across the interface $\gamma_{i,i+1}$. If we consider three dimensions we say that $|\gamma_{i,i+1}|$ is the area of $\gamma_{i,i+1}$ while it is the length in two dimension.

We now want to find an approximation for the permeability **K**. There are many different averaging methods that can be used, but the harmonic average is used in TPFA. This stems from the following proposition.

**Proposition 2.2.2.** Harmonic average
*For one-dimensional flow the results in Equation* (2.16) *becomes exact if the harmonic average:*

$$\mathbf{K}_{i+1/2} = (\Delta x_{i+1} + \Delta x_i)\left(\frac{\Delta x_{i+1}}{\mathbf{K}_{i+1}} + \frac{\Delta x_i}{\mathbf{K}_i}\right)^{-1}, \tag{2.18}$$

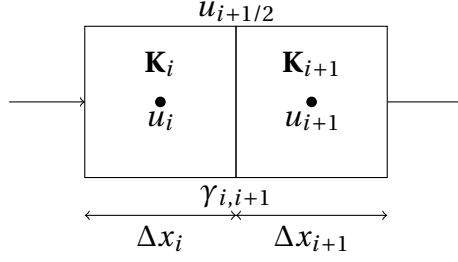*is being used to approximate the permeability.*

8

**Figure 2.3:** *Approximation of the permeability.*

*Proof.* For the domain above we have three different expressions for the flux through the interface $\gamma_{i,i+1}$:

$$
\begin{aligned}
\mathbf{f}^1_{i,i+1} &= -\frac{2(u_{i+1/2} - u_i)}{\Delta x_i} \int_{\gamma_{i,i+1}} \frac{\mathbf{K}_i}{\mu} \cdot \vec{n} dv, \\
\mathbf{f}^2_{i,i+1} &= -\frac{2(u_{i+1} - u_{i+1/2})}{\Delta x_{i+1}} \int_{\gamma_{i,i+1}} \frac{\mathbf{K}_{i+1}}{\mu} \cdot \vec{n} dv, \\
\mathbf{f}^3_{i,i+1} &= -\frac{2(u_{i+1} - u_i)}{\Delta x_{i+1} + \Delta x_i} \int_{\gamma_{i,i+1}} \frac{\mathbf{K}_{i+1/2}}{\mu} \cdot \vec{n} dv.
\end{aligned}
$$

The permeabilities are now constant within its region, and we can write:

$$
\begin{aligned}
\mathbf{f}^1_{i,i+1} &= -\frac{2(u_{i+1/2} - u_i)}{\Delta x_i} \cdot \frac{|\gamma_{i,i+1}|\mathbf{K}_i}{\mu}, \\
\mathbf{f}^2_{i,i+1} &= -\frac{2(u_{i+1} - u_{i+1/2})}{\Delta x_{i+1}} \cdot \frac{|\gamma_{i,i+1}|\mathbf{K}_{i+1}}{\mu}, \\
\mathbf{f}^3_{i,i+1} &= -\frac{2(u_{i+1} - u_i)}{\Delta x_{i+1} + \Delta x_i} \cdot \frac{|\gamma_{i,i+1}|\mathbf{K}_{i+1/2}}{\mu}.
\end{aligned}
$$

If we have one-dimensional flow we have $\mathbf{f}^1_{i,i+1} = \mathbf{f}^2_{i,i+1} = \mathbf{f}^3_{i,i+1} = \mathbf{f}_{i,i+1}$ and hence we get:

$$
\frac{\mathbf{f}_{i,i+1}\Delta x_i}{|\gamma_{i,i+1}|\frac{\mathbf{K}_i}{\mu}} + \frac{\mathbf{f}_{i,i+1}\Delta x_{i+1}}{|\gamma_{i,i+1}|\frac{\mathbf{K}_{i+1}}{\mu}} = -2(u_{i+1} - u_i) = \frac{\mathbf{f}_{i,i+1}(\Delta x_{i+1} + \Delta x_i)}{|\gamma_{i,i+1}|\frac{\mathbf{K}_{i+1/2}}{\mu}}.
$$

This leads to:

$$
\frac{\Delta x_i}{\mathbf{K}_i} + \frac{\Delta x_{i+1}}{\mathbf{K}_{i+1}} = \frac{\Delta x_{i+1} + \Delta x_i}{\mathbf{K}_{i+1/2}},
$$

$$
\mathbf{K}_{i+1/2} = (\Delta x_{i+1} + \Delta x_i)\left(\frac{\Delta x_{i+1}}{\mathbf{K}_{i+1}} + \frac{\Delta x_i}{\mathbf{K}_i}\right)^{-1},
$$

which is the harmonic average. $\qquad \square$

The mobility, $\lambda_{i+1/2}$, is defined as $\frac{\mathbf{K}_{i+1/2}}{\mu}$ which becomes:

$$
\begin{aligned}
\lambda_{i+1/2} &= (\Delta x_{i+1} + \Delta x_i)\left(\frac{\mu \Delta x_{i+1}}{\mathbf{K}_{i+1}} + \frac{\mu \Delta x_i}{\mathbf{K}_i}\right)^{-1} \\
&= (\Delta x_{i+1} + \Delta x_i)\left(\frac{\Delta x_{i+1}}{\lambda_{i+1}} + \frac{\Delta x_i}{\lambda_i}\right)^{-1}.
\end{aligned}
$$

Using this and inserting it into Equation (2.16) yields the definition of the two-point flux-approximation.

**Definition 2.2.2.** Two-point flux-approximation
*The flux $f_{i,i+1}$ between cell $i$ and cell $i+1$ can be approximated by:*

$$
f_{i,i+1} = 2|\gamma_{i,i+1}|\left(\frac{\Delta x_{i+1}}{\lambda_{i+1}} + \frac{\Delta x_i}{\lambda_i}\right)^{-1}(u_i - u_{i+1}). \tag{2.19}
$$

The term without the cell potentials, $(u_i - u_{i+1})$, is called the transmissibility, which in general can be written

$$
T_{i,j} = 2|\gamma_{i,j}|\left(\frac{\Delta x_i}{\lambda_i} + \frac{\Delta x_j}{\lambda_j}\right)^{-1}. \tag{2.20}
$$

TPFA tries to find a $u$ which is cell-wise constant and solves the following set of equations.

$$
\sum_j T_{i,j}(u_i - u_j) = \int_{\Omega_i} \frac{q}{\rho} dx,
$$
$$
\text{for all cells } \Omega_i \in \Omega. \tag{2.21}
$$

The transmissibility matrix, $\mathbf{T}$ is diagonal for TPFA. This method is, however, only convergent for cells where the grid is $\mathbf{K}$-orthogonal.

In the next sections, we will consider some different approximation methods, and we will find another expression for the transmissibility for TPFA, expressed in terms of half-transmissibilities, in order to better compare these methods.

We consider two cells, cell $i$ and cell $j$, and they share a face, face $k$. If we have a regular cartesian grid in three dimensions, our system will have 11 unique faces. If we look at cell $i$, six faces make up this cell, and six faces make up cell $j$. If we consider one cell, we will call the faces belonging to this cell half-faces, and thus, our system have 12 half-faces where two of them represent face $k$, but one holds the properties of cell $i$ and the other one the properties of cell $j$. A half-transmissibility is thus the transmissibility corresponding to a half-face.

If we only consider cell $i$, we can look at the expression for the flux $\mathbf{f}^{\mathrm{l}}_{i,i+1}$:

$$
\begin{aligned}
\mathbf{f}^{\mathrm{l}}_{i,i+1} &= -2|\gamma_{i,i+1}|\frac{(u_{i+1/2} - u_i)}{\Delta x_i}\frac{\mathbf{K}_i}{\mu}, \\
\mathbf{f}^{\mathrm{l}}_{i,i+1} &= T_i(i+1)(u_i - u_{i+1/2}), \\
T_i(i+1) &= 2|\gamma_{i,i+1}|\left(\frac{\Delta x_i}{\lambda_i}\right)^{-1}.
\end{aligned}
\tag{2.22}
$$

This is the flux through the interface between cell $i$ and cell $i+1$, but seen from cell $i$. As one can see the transmissibility only involves properties of cell $i$. This transmissibility is a half-transmissibility, and when considering TPFA, one cell has as many half transmissibilities as it has faces, and $T_i(i+1)$ represents the half-transmissibility for cell $i$ coming from the face which cell $i$ shares with cell $i+1$. Hence, one can write as in [5],

$$
\mathbf{f}_i = \mathbf{T}_i(\vec{e}_i u_i - \boldsymbol{\pi}_i).
\tag{2.23}
$$

Where $\mathbf{T}_i$ is a vector consisting of the half-transmissibilities connected to cell $i$, $\boldsymbol{\pi}_i$ is a vector representing the potentials at the face centroids of cell $i$, and $u_i$ is the potential at the cell centroid of cell $i$.

We now need the following proposition to be true:

**Proposition 2.2.3.** *Writing TPFA in terms of half-transmissibilities as done in Equation (2.23) is consistent with the regular cell-centred formulation, which is a harmonic average of two half-transmissibilities.*

*Proof.* To see that Equation (2.23) is consistent with (2.19), we have that $\mathbf{f}_i(i+1)$ is the $(i+1)$'th element of the vector $\mathbf{f}_i$, i.e., the contribution of the flux through the interface $\gamma_{i,i+1}$ from cell $i$, and $\mathbf{f}_{i+1}(i)$ is the $i$'th element of the vector $\mathbf{f}_{i+1}$, i.e., the contribution of the flux through the interface $\gamma_{i,i+1}$ from cell $i+1$:

$$
\begin{aligned}
\mathbf{f}_i(i+1) &= 2|\gamma_{i,i+1}|\frac{\lambda_i}{\Delta x_i}(u_i - \boldsymbol{\pi}_i(i+1)), \\
\mathbf{f}_{i+1}(i) &= 2|\gamma_{i,i+1}|\frac{\lambda_{i+1}}{\Delta x_{i+1}}(u_{i+1} - \boldsymbol{\pi}_{i+1}(i)).
\end{aligned}
$$

Here, $\boldsymbol{\pi}_i(i+1) = \boldsymbol{\pi}_{i+1}(i)$ and in the following we will call it $\pi$,

$$
\begin{aligned}
\mathbf{f}_i(i+1) &= -\mathbf{f}_{i+1}(i), \\
\frac{\lambda_i}{\Delta x_i}(u_i - \pi) &= \frac{\lambda_{i+1}}{\Delta x_{i+1}}(\pi - u_{i+1}), \\
\pi\left(\frac{\Delta x_{i+1}}{\lambda_{i+1}} + \frac{\Delta x_i}{\lambda_i}\right) &= \frac{\Delta x_i}{\lambda_i}u_{i+1} + \frac{\lambda_{i+1}}{\Delta x_{i+1}}u_i.
\end{aligned}
$$

11

Inserting $\pi = \left( \frac{\Delta x_i}{\lambda_i} u_{i+1} + \frac{\lambda_{i+1}}{\Delta x_{i+1}} u_i \right) \left( \frac{\Delta x_{i+1}}{\lambda_{i+1}} + \frac{\Delta x_i}{\lambda_i} \right)^{-1}$ into $\mathbf{f}_i(i+1)$ we get:

$$
\begin{aligned}
\mathbf{f}_i(i+1) &= 2|\gamma_{i,i+1}| \left( \frac{\lambda_i}{\Delta x_i} u_i - \frac{\lambda_i}{\Delta x_i} \left( \frac{\Delta x_i}{\lambda_i} u_{i+1} + \frac{\lambda_{i+1}}{\Delta x_{i+1}} u_i \right) \left( \frac{\Delta x_{i+1}}{\lambda_{i+1}} + \frac{\Delta x_i}{\lambda_i} \right)^{-1} \right) \\
&= 2|\gamma_{i,i+1}| \left( \frac{\Delta x_{i+1}}{\lambda_{i+1}} \frac{\lambda_i}{\Delta x_i} u_i + u_i - u_{i+1} - \frac{\Delta x_{i+1}}{\lambda_{i+1}} \frac{\lambda_i}{\Delta x_i} u_i \right) \left( \frac{\Delta x_{i+1}}{\lambda_{i+1}} + \frac{\Delta x_i}{\lambda_i} \right)^{-1} \\
&= 2|\gamma_{i,i+1}| (u_i - u_{i+1}) \left( \frac{\Delta x_{i+1}}{\lambda_{i+1}} + \frac{\Delta x_i}{\lambda_i} \right)^{-1}.
\end{aligned}
\tag{2.24}
$$

$\square$

We note that this is the same as (2.19). However, to solve the system in Equation (2.23) is more computationally costly than to solve (2.21) since we now have an edge centred system instead of a cell centred.

## 2.3 Mimetic discretisation methods

In this section, we will present the mimetic method. The mimetic method is a finite difference method, i.e., mimetic finite difference method; (MFD). We will first present the method based on [11], and thereafter we will show how the inner product matrices, $\mathbf{M}$, are made based on [5].

As before, we have Darcy's law, Equation (2.7), which in simplified form can be written as:

$$
\begin{aligned}
\vec{f} &= -\mathbf{K}\nabla u, \\
\nabla \cdot \vec{f} &= \frac{q}{\rho}.
\end{aligned}
\tag{2.25}
$$

where $\vec{f}$ is the flux and $u$ is the potential.

If we have Dirichlet boundary conditions, i.e., $\vec{f} \cdot \vec{n} = 0$ on $\partial\Omega$, then Green's formula will give us the following:

$$
\int_\Omega u \nabla \cdot \vec{f} \, dx + \int_\Omega \vec{f} \cdot \mathbf{K}^{-1}(\mathbf{K}\nabla u) = 0.
\tag{2.26}
$$

We want to discretise Green's formula, and we will define scalar products in the discrete spaces which we will use. We will consider the space $Q^h$ which is a space consisting of discrete potentials that are constant on each element $E$, and for every $\mathbf{q} \in Q^h$ we say that $q_E$ is its value on element $E$. The space $X^h$ is a space of discrete velocities,
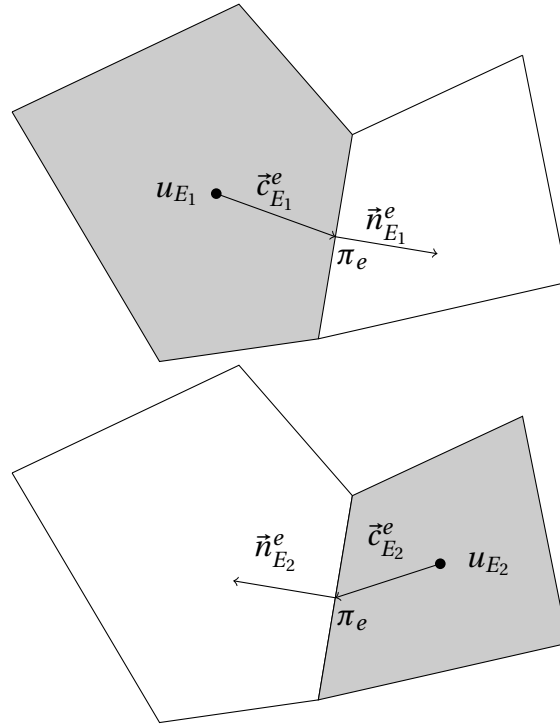
12

**Figure 2.4:** *Pictorial explanation of quantities used to define the mimetic inner product for cell $E_1$ on the top and $E_2$ on the bottom.*

and for every face $e$ of element $E$ we associate the vector field $f_E^e \vec{n}_E^e$. The vector $\vec{n}_E^e$ is the unit outward normal to face $e$ of element $E$, see Figure 2.4. Hence for a face $e$ that is shared by element $E_1$ and $E2$ we according to [11] get:

$$f_{E_1}^e = -f_{E_2}^e. \tag{2.27}$$

We will now state the discrete scalar products in the spaces $Q^h$ and $X^h$. For elements in the space $Q^h$ we, according to [7], have the following definition:

**Definition 2.3.1.** *For any $q \in L^1(\Omega)$ we define $q^I \in Q^h$ such that:*

$$(q^I)_E = \frac{1}{|E|} \int_E q(x)dx \quad \forall E \in \Omega^h. \tag{2.28}$$

*Where $|E|$ is the volume of element $E$ in three dimensions and the area of element $E$ if we are in two dimensions.*

Hence we define the following scalar product:

**Definition 2.3.2.** *For $\mathbf{u} = u^I, \mathbf{q} = q^I \in Q^h$ we have the the following scalar product:*

$$[\mathbf{u}, \mathbf{q}]_{Q^h} = \sum_{E \in \Omega_h} |E| u_E q_E. \tag{2.29}$$

We have the following definition for elements in the space $X^h$:

13

**Definition 2.3.3.** *For any* $\vec{v} \in \{\vec{v} : \vec{v} \in (L^s(\Omega))^d, s > 2, \nabla \cdot \vec{v} \in L^2(\Omega)\}$ *we define* $\vec{v}^I \in X^h$:

$$(\vec{v}^I)_E^e = \frac{1}{|e|} \int_e \vec{v} \cdot \vec{n}_E^e ds, \quad \forall E \in \Omega^h, \quad \forall e \in \partial E. \tag{2.30}$$

This leads to the following scalar product in $X^h$:

**Definition 2.3.4.** *For* $\mathbf{f} = \vec{f}^I, \mathbf{v} = \vec{v}^I \in X^h$ *we have:*

$$[\mathbf{f}, \mathbf{v}]_{X^h} = \sum_{E \in \Omega_h} [\mathbf{f}, \mathbf{v}]_E, \tag{2.31}$$

*where*

$$[\mathbf{f}, \mathbf{v}]_E = \sum_{s,r=1}^{k_E} \mathbf{M}_{E,s,r} f_E^{e_s} v_E^{e_r}, \tag{2.32}$$

*where $k_E$ is the number of faces belonging to element E. The matrix $\mathbf{M}_E$ is an inner product matrix for element E. This means that $\mathbf{M}_E$ is symmetric and positive-definite.*

We also need to discretise the divergence operator. We let $Hf = \nabla \cdot \vec{f}$:

**Definition 2.3.5.** *If we have an element* $\mathbf{v} \in X^h$ *and take the divergence we get an element* $\mathbf{Hv} \in Q^h$. *We define this for each E as:*

$$(\mathbf{Hv})_E := \frac{1}{|E|} \sum_{i=1}^{k_E} |e_i| v_E^{e_i}, \tag{2.33}$$

*where $|e_i|$ is the area of the i'th face of element E in three dimension and the length in two dimensions.*

We will use this to prove the following proposition:

**Proposition 2.3.1.** *The approximation of Equation (2.26) can be written in discretised form as:*

$$\sum_{E \in \Omega_h} |E| u_E (\mathbf{Hf})_E + \sum_{E \in \Omega_h} \sum_{s,r=1}^{k_E} \mathbf{M}_{E,s,r} f_E^{e_s} (Gu)_E^{e_r} = 0. \tag{2.34}$$

*Proof.* We approximate the first integral in Equation (2.26) by the scalar product in $Q^h$, and we get:

$$\int_\Omega u \nabla \cdot \vec{f} dx \approx [\mathbf{u}, \mathbf{Hf}]_{Q^h} = \sum_{E \in \Omega_h} |E| u_E (\mathbf{Hf})_E. \tag{2.35}$$

We let $Gu = \mathbf{K}\nabla u$ and then we approximate the second integral in Equation 2.26 by the scalar product in $X^h$:

$$\int_\Omega \vec{f} \cdot \mathbf{K}^{-1} (\mathbf{K}\nabla u) \approx [\mathbf{f}, \mathbf{Gu}]_{X^h} = \sum_{E \in \Omega_h} \sum_{s,r=1}^{k_E} \mathbf{M}_{E,s,r} f_E^{e_s} (Gu)_E^{e_r}, \tag{2.36}$$

$\square$

In discretised form we can write Equation (2.25) as:

$$\mathbf{f} = -\mathbf{G}u,$$
$$\mathbf{H}\mathbf{f} = \frac{\mathbf{q}}{\rho}. \tag{2.37}$$

We now want to find the inner product matrix $\mathbf{M}$ and the transmissibility matrix $\mathbf{T}$ which is the inverse of $\mathbf{M}$. The properties of $\mathbf{M}$ are that the matrix is symmetric positive-definite, and it is constructed in such a way that the mimetic method is exact for linear pressure fields. According to [5] we want to have a solution on the form:

$$\mathbf{f}_E = \mathbf{T}_E(\vec{e}_E u_E - \boldsymbol{\pi}_E). \tag{2.38}$$

This can also be written as

$$\mathbf{M}_E\mathbf{f}_E = \vec{e}_E u_E - \boldsymbol{\pi}_E. \tag{2.39}$$

The mass flux is the rate of mass flowing through a unit area, and hence one can write:

$$\begin{aligned} f_E^e &= -\vec{n}_E^e(Gu)_E^e \\ &= -\vec{n}_E^e(\mathbf{K}\nabla u)_E^e. \end{aligned} \tag{2.40}$$

From [11] we get the following identity:

$$\int_{\partial E} (\mathbf{K}\nabla x_i) \cdot \vec{n} x_j \mathrm{d}s = \int_E \mathbf{K}\nabla x_i \cdot \nabla x_j \mathrm{d}V = |E|\mathbf{K}_{ij}, \tag{2.41}$$

where $(x_i, ..., x_d)$ are the cartesian coordinates in $d$ dimensions and the origin is set to be at the center of mass of $E$. We then let:

$$\mathbf{C}_{s,i} = \int_{e_s} x_i \mathrm{d}s, \quad \text{and} \quad \mathbf{N}_{s,i} = (\nabla x_i) \cdot \vec{n}_E^{e_s}. \tag{2.42}$$

This means that the vector pointing from the cell centroid to the face centroid is $\vec{c}_E^e$. For each cell these vectors are placed in a matrix $\mathbf{C}$, where $\mathbf{c}_s$ is the $s$'th row of $\mathbf{C}$ and this is $(\vec{c}_E^{e_s})^T$. We also find the area weighted normal vectors of each face and then we multiply by 1 or $-1$ such that the direction of the vectors are pointing outwards of the respective cell. Hence for a face that belongs to two different cells, say cell $E_k$ and cell $E_j$ the sign of $\vec{n}_{E_k}^e$ is different from $\vec{n}_{E_j}^e$. These are placed in the matrix $\mathbf{N}$ in the same manner as the vectors were placed in $\mathbf{C}$. The relationship between $\mathbf{N}$ and $\mathbf{C}$ is explained in [11] as:

$$\mathbf{C}^{\mathbf{T}}\mathbf{N} = \mathbf{I}(|E_i|), \tag{2.43}$$

where $\mathbf{I}$ is the identity matrix. This follows from Equation (2.41).

We now assume a linear pressure field and then the drop in the potential is:

$$u_E - \boldsymbol{\pi}_E(e) = \vec{c}_E^e \cdot \nabla u, \tag{2.44}$$

where $u_E$ is the potential at the cell centroid of cell $E$, and $\boldsymbol{\pi}_E(e)$ is the potential at the face centroid of face $e$.

We need an inner product matrix $\mathbf{M}$ that fulfills Equations (2.39), hence we state the following proposition:

**Proposition 2.3.2.** *The inner product matrix* $\mathbf{M}$*:*

$$\mathbf{M} = \frac{1}{|E_i|}\mathbf{CK}^{-1}\mathbf{C}^{\mathbf{T}} + \mathbf{M_2}, \tag{2.45}$$

*fulfills the solution stated in Equation (2.39), where* $\mathbf{M_2}N = 0$*.*

*Proof.* Combining Equations (2.39)-(2.44) we get:

$$\begin{aligned} \mathbf{Mf} = \mathbf{MNK}\nabla u &= \mathbf{u} - \boldsymbol{\pi} = \mathbf{C} \cdot \nabla u, \\ \mathbf{MNK} &= \mathbf{C}. \end{aligned} \tag{2.46}$$

Inserting the results into Equation (2.40) gives us:

$$\begin{aligned} \mathbf{F} = \mathbf{NK}\nabla u &= \mathbf{T}(\mathbf{u} - \boldsymbol{\pi}) = \mathbf{TC}\nabla u, \\ \mathbf{NK} &= \mathbf{TC}. \end{aligned} \tag{2.47}$$

For one $d$-dimensional cell with $n$ faces, $\mathbf{C}$ and $\mathbf{N}$ will be $n \times d$ matrices.

Multiplying Equation (2.46) with $\mathbf{K}^{-1}\mathbf{C}^{\mathbf{T}}\mathbf{N} = \mathbf{K}^{-1}\mathbf{I}(|E_i|)$ gives the following:

$$\begin{aligned} \mathbf{MNKK}^{-1}(|E_i|) &= \mathbf{CK}^{-1}\mathbf{C}^{\mathbf{T}}\mathbf{N}, \\ \mathbf{MN} &= \frac{1}{|E_i|}\mathbf{CK}^{-1}\mathbf{C}^{\mathbf{T}}\mathbf{N}. \end{aligned} \tag{2.48}$$

There is not only one unique $\mathbf{M}$ satisfying Equation (2.48), but they all have the form

$$\mathbf{M} = \frac{1}{|E_i|}\mathbf{CK}^{-1}\mathbf{C}^{\mathbf{T}} + \mathbf{M_2}, \tag{2.49}$$

$$\text{where } \mathbf{M_2N} = 0.$$

Generally, according to [5] we can write

$$\mathbf{M_2} = \mathbf{Q}_{\mathbf{N}}^{\perp}\mathbf{S_M}\mathbf{Q}_{\mathbf{N}}^{\perp^{\mathbf{T}}}, \tag{2.50}$$

where $\mathbf{Q}_{\mathbf{N}}^{\perp^{\mathbf{T}}}$ is an orthonormal basis for the nullspace of $\mathbf{N}$, and $\mathbf{S_M}$ needs to be a symmetric positive-definite matrix such that $\mathbf{M_2}$ is a symmetric positive-definite matrix. $\quad\square$

The matrix $\mathbf{M}$ is symmetric and positive-definite. We also need to find the transmissibility matrix $\mathbf{T}$

**Proposition 2.3.3.** *The transmissibility matrix* $\mathbf{T}$,

$$\mathbf{T} = \frac{1}{|E_i|}\mathbf{N}\mathbf{K}\mathbf{N}^{\mathbf{T}} + \mathbf{T_2}, \qquad (2.51)$$

*fulfills the solution stated in Equation* (2.38), *where* $\mathbf{T_2}\mathbf{C} = 0$.

*Proof.* The matrix $\mathbf{C}^{\mathbf{T}}\mathbf{N} = \mathbf{I}(|E_i|)$ is a symmetric matrix, hence

$$\mathbf{C}^{\mathbf{T}}\mathbf{N} = \mathbf{N}^{\mathbf{T}}\mathbf{C} = \mathbf{I}(|E_i|). \qquad (2.52)$$

Hence, multiplying Equation (2.47) with $\mathbf{N}^{\mathbf{T}}\mathbf{C}$ gives:

$$
\begin{aligned}
\mathbf{T}\mathbf{C}(|E_i|) &= \mathbf{N}\mathbf{K}\mathbf{N}^{\mathbf{T}}\mathbf{C}, \\
\mathbf{T}\mathbf{C} &= \frac{1}{|E_i|}\mathbf{N}\mathbf{K}\mathbf{N}^{\mathbf{T}}\mathbf{C}.
\end{aligned}
\qquad (2.53)
$$

Again, there is not one unique $\mathbf{T}$, but all the alternatives have the form:

$$
\mathbf{T} = \frac{1}{|E_i|}\mathbf{N}\mathbf{K}\mathbf{N}^{\mathbf{T}} + \mathbf{T_2}, \qquad (2.54)
$$
$$
\text{where } \mathbf{T_2}\mathbf{C} = 0.
$$

Generally one can write:

$$\mathbf{T} = \frac{1}{|E_i|}\mathbf{N}\mathbf{K}\mathbf{N}^{\mathbf{T}} + \mathbf{Q}_{\mathbf{C}}^{\perp}\mathbf{S_T}\mathbf{Q}_{\mathbf{C}}^{\perp^{\mathbf{T}}}, \qquad (2.55)$$

where $\mathbf{Q}_{\mathbf{C}}^{\perp^{\mathbf{T}}}$ is an orthonormal basis for the nullspace of $\mathbf{C}$, and $\mathbf{S_T}$ is a symmetric positive-definite matrix. $\qquad \square$

The default mimetic inner product in MRST is `ip_simple`:

$$
\begin{aligned}
\mathbf{Q} &= \operatorname{orth}(\mathbf{A}^{-1}\mathbf{N}), \\
\mathbf{M} &= \frac{1}{|E_i|}\mathbf{C}\mathbf{K}^{-1}\mathbf{C}^{\mathbf{T}} + \frac{\mathbf{I}(|E_i|)}{6tr(\mathbf{K})}\mathbf{A}^{-1}(\mathbf{I} - \mathbf{Q}\mathbf{Q}^{\mathbf{T}})\mathbf{A}^{-1},
\end{aligned}
\qquad (2.56)
$$

where $\mathbf{A}$ is a diagonal matrix and $a_{ii}$ is the area of the $i$'th face.

The corresponding inverse, the transmissibility matrix that beholds the same qualities as the inverse of $\mathbf{M}$ is:

$$
\begin{aligned}
\mathbf{Q} &= \text{orth}(\mathbf{AC}), \\
\mathbf{T} &= \frac{1}{|E_i|}\left(\mathbf{NKN^T} + 6\,tr(\mathbf{K})\mathbf{A}(\mathbf{I} - \mathbf{QQ^T})\mathbf{A}\right).
\end{aligned}
\tag{2.57}
$$

## 2.4 Multipoint flux approximation methods

It is hardly ever possible to construct **K**-orthogonal grids. We need more points to develop a consistent flux approximation for grids that are not **K**-orthogonal. We have already presented the theory behind the mimetic discretisation methods, but there are also another group of approximations which are consistent for grids that are not **K**-orthogonal. These are called multipoint flux approximations; (MPFA). The main difference between mimetic discretisation and MPFA is that MPFA can be reduced to a system for grid block pressures rather than the grid block interface pressures as in the mimetic method. I.e., the fluxes are calculated in terms of grid block pressure differences for MPFA. The mimetic inner product for one cell is calculated by using properties associated with this cell while the MPFA inner product is calculated by considering corners and the faces associated with this corner, and the faces may thus belong to different cells. MPFA may also be reduced to a cell-centred system while the mimetic methods are edge-centred.

We will present the MPFA-O method. The calculations and notations are based on [3] and [6]

We still assume that the flux through a surface $\gamma_{i,i+1}$ between cell $i$ and cell $i+1$ equals:

$$
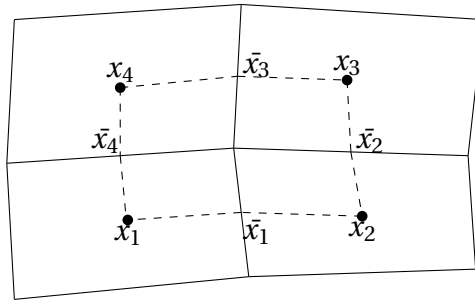f_{i,i+1} = -\int_{\gamma_{i,i+1}} (\frac{\mathbf{K}}{\mu}\nabla\vec{u})\cdot\vec{n}dv.
\tag{2.58}
$$



**Figure 2.5:** *Quadrilateral grid.*

Consider the two-dimensional grid in Figure 2.5. The grid consists of four cells with mid-points $x_1$, $x_2$, $x_3$, $x_4$. We draw lines between the mid-points of the cells and the mid-points of the edges marked as $\bar{x}_1$, $\bar{x}_2$, $\bar{x}_3$, $\bar{x}_4$. Consider the polygon with corners $x_1\bar{x}_1x_2\bar{x}_2x_3\bar{x}_3x_4\bar{x}_4$, this is referred to as an interaction region. Inside the polygon there

are four half-edges and we want to find the flux over these half-edges. When this is done for one corner one can proceed and find the fluxes over the other half-edges in the grid.

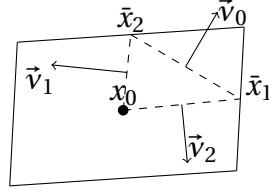For one cell in two dimensions we can consider Figure 2.6.



**Figure 2.6:** *One cell in 2D.*

There is a normal-vector perpendicular to the line $x_0\bar{x}_1$ and this is called $\vec{v}_2$. There is also a normal-vector perpendicular to the line $x_0\bar{x}_2$, and this is called $\vec{v}_1$, and a normal-vector perpendicular to the line $\bar{x}_2\bar{x}_1$ and this is called $\vec{v}_0$. The sum of the normal-vectors is 0, and hence $\vec{v}_0 = -(\vec{v}_1 + \vec{v}_2)$

The triangle will in three dimensions be a tetrahedron, and we will also have an extra point, $\bar{x}_3$. We now have four normal-vectors and these are defined as:

$$
\begin{aligned}
\vec{v}_1 &= (\bar{x}_2 - x_0) \times (\bar{x}_3 - x_0), \\
\vec{v}_2 &= (\bar{x}_1 - x_0) \times (\bar{x}_3 - x_0), \\
\vec{v}_3 &= (\bar{x}_1 - x_0) \times (\bar{x}_2 - x_0), \\
\vec{v}_0 &= -(\vec{v}_1 + \vec{v}_2 + \vec{v}_3).
\end{aligned}
\tag{2.59}
$$

**Lemma 2.4.1.** *For a tetrahedron with corners $x_0$, $\bar{x}_1$, $\bar{x}_2$, $\bar{x}_3$, any linear function can be written as:*

$$
u(x) = \sum_{i=0}^{3} \bar{u}_i \phi_i(x),
\tag{2.60}
$$

*where $\phi_i(x)$ is the linear basis function, $\phi_i(x_j) = \delta_{i,j}$.*

In our case, $u$, is the potential for the cell and we consider it to be linear within this cell. The value of $u$ at corner $\bar{x}_i$ is $\bar{u}_i$ where $\bar{x}_0 = x_0$ and hence $\bar{u}_0 = u_0$.

From [3] it is known that:

$$
\nabla \phi_i = \frac{1}{V} v_i,
\tag{2.61}
$$

and $V = (\bar{x}_1 - x_0)(\bar{x}_2 - x_0)(\bar{x}_3 - x_0)$, where $V$ is 6 times the volume of the tetrahedron.

We now want to find the flux through one subinterface and we will derive the following proposition:

**Proposition 2.4.1.** *If we have a linear drop in the pressure, the flux through a subinterface $k$ belonging to halfface $i$ of cell $j$ can be written as:*

$$f_k = -\frac{1}{\mu V_{jk}} \sum_{i=1}^{3} \mathbf{K}_j \vec{v}_{ji} (\bar{u}_{ji} - u_j) \cdot \vec{n}_k. \tag{2.62}$$

*Proof.* We begin by taking the divergence of $u$ which gives us:

$$
\begin{aligned}
\nabla u &= \frac{1}{V} \sum_{i=0}^{3} \bar{u}_i \vec{v}_i \\
&= \frac{1}{V} [-u_0(\vec{v}_1 + \vec{v}_2 + \vec{v}_3) + \bar{u}_1 \vec{v}_1 + \bar{u}_2 \vec{v}_2 + \bar{u}_3 \vec{v}_3] \\
&= \frac{1}{V} [\vec{v}_1(\bar{u}_1 - u_0) + \vec{v}_2(\bar{u}_2 - u_0) + \vec{v}_3(\bar{u}_3 - u_0)] \\
&= \frac{1}{V} \sum_{i=1}^{3} \vec{v}_i(\bar{u}_i - u_0). 
\end{aligned}
\tag{2.63}
$$

This expression explains in three dimension only $\nabla u$ for one quarter of the surface $\gamma_{i,i+1}$ and this is subsurface $k$. By inserting (2.63) into Equation (2.58), we get:

$$f_k = -\frac{1}{\mu V_{jk}} \sum_{i=1}^{3} \mathbf{K}_j \vec{v}_{ji} (\bar{u}_{ji} - u_j) \cdot \vec{n}_k. \tag{2.64}$$

The cell is $j$, the subinterface, is $k$, and the local cell surface is $i$, and this is what we proposed. The volume $V_{jk}$ is 6 times the volume of the tetrahedron made for subinterface $k$ in cell $j$: □

For simplicity we can write Equation (2.62) as:

$$f_k = \sum_{i=1}^{d} \omega_{kji}(\bar{u}_{ji} - u_j), \tag{2.65}$$

where $d$ is the dimension, and

$$\omega_{kji} = -\frac{n_k^T \mathbf{K_j} \vec{v}_{ji}}{\mu V_j k}. \tag{2.66}$$

We will now consider a system of eight cells that all have one mutual corner, and we want to find an expression in matrix form collecting all of the different $f_k$, so that we can write our system of equations for the interaction region around the corner on the form $\mathbf{f} = \mathbf{Tu}$.

Consider Figure 2.7, and note the centre of the figure, i.e., the point that is shared by all of the eight cells $O$. There are 12 interfaces meeting at this point. Each cell has a midpoint which is called $x_j$ for cell $j$, $j = 1,...,8$, the potential at these points are denoted $u_j$. Each cell has three faces that contributes to the flux through $O$, and each
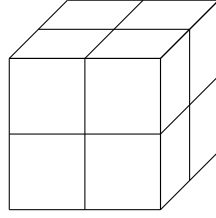
**Figure 2.7:** *Three dimensional cartesian grid.*

of these faces has a centre point. For cell $j$ these points are called $\bar{x}_{ji}$, $i = 1, 2, 3$ and has potentials $\bar{u}_{ji}$. We can consider $i$ as being 3 in the xy-plane, 2 in the xz-plane and 1 in the yz-plane. To get a better illustration of the interfaces, we will look at the cross-sections of the domain.
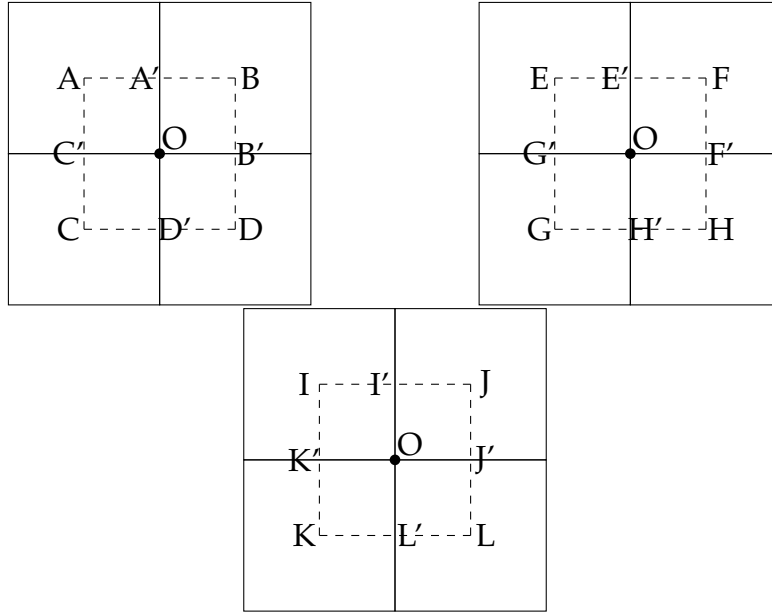


**Figure 2.8:** *Cross-sections, xy-plane, xz-plane, yz-plane.*

$$
\begin{aligned}
A &= \bar{x}_{13} = \bar{x}_{53}, \quad B = \bar{x}_{23} = \bar{x}_{63}, \quad C = \bar{x}_{33} = \bar{x}_{73}, \quad D = \bar{x}_{43} = \bar{x}_{83}. \\
E &= \bar{x}_{12} = \bar{x}_{32}, \quad F = \bar{x}_{22} = \bar{x}_{42}, \quad G = \bar{x}_{52} = \bar{x}_{72}, \quad H = \bar{x}_{62} = \bar{x}_{82}. \\
I &= \bar{x}_{31} = \bar{x}_{41}, \quad J = \bar{x}_{11} = \bar{x}_{21}, \quad K = \bar{x}_{71} = \bar{x}_{81}, \quad L = \bar{x}_{51} = \bar{x}_{61}.
\end{aligned}
$$

The respective potentials have the same indices, but since some are equal we can say that:

$$
\begin{aligned}
\bar{u}_A &= \bar{u}_1, \quad \bar{u}_B = \bar{u}_2, \quad \bar{u}_C = \bar{u}_3, \quad \bar{u}_D = \bar{u}_4, \\
\bar{u}_E &= \bar{u}_5, \quad \bar{u}_F = \bar{u}_6, \quad \bar{u}_G = \bar{u}_7, \quad \bar{u}_H = \bar{u}_8, \\
\bar{u}_I &= \bar{u}_9, \quad \bar{u}_J = \bar{u}_{10}, \quad \bar{u}_K = \bar{u}_{11}, \quad \bar{u}_L = \bar{u}_{12}.
\end{aligned}
\tag{2.67}
$$

The flux through the subinterface $OA'$, equals the sum of the fluxes through the interfaces $x_1 A$, $x_1 E$ and $x_1 J$. This is the same as the sum of fluxes through the interfaces

$x_2B$, $x_2F$ and $x_2J$. We call subinterface $OA'$ subinterface 1, i.e., $k = 1$ in Equation (2.66). Hence, we can write:

$$\omega_{113}(\bar{u}_1 - u_1) + \omega_{112}(\bar{u}_5 - u_1) + \omega_{111}(\bar{u}_{10} - u_1) = \omega_{123}(\bar{u}_2 - u_2) + \omega_{122}(\bar{u}_6 - u_2) + \omega_{121}(\bar{u}_{10} - u_2).$$
(2.68)

We have 11 similar expressions for the other subinterfaces.

The matrix form of Equation (2.65) can be written as:

$$\mathbf{f} = \mathbf{Cv} - \mathbf{Du},$$
(2.69)

where $\mathbf{v} = [\bar{u}_1, \ldots, \bar{u}_{12}]$ and $\mathbf{u} = [u_1, \ldots, u_8]$. The system of equations can be written as

$$\mathbf{Av} = \mathbf{Bu}.$$
(2.70)

Inserting Equation (2.70) into Equation (2.69) we get:

$$
\begin{aligned}
\mathbf{f} &= \left(\mathbf{CA}^{-1}\mathbf{B} - \mathbf{D}\right)\mathbf{u}, \\
\mathbf{f} &= \mathbf{Tu}, \\
\mathbf{T} &= \mathbf{CA}^{-1}\mathbf{B} - \mathbf{D}.
\end{aligned}
$$
(2.71)
(2.72)

Here, $\mathbf{T}$ is the transmissibility matrix for one interaction region. If we find solutions for the four interaction regions containing parts of a specific interface and add the fluxes of the subinterfaces, we find the transmissibility coefficients for this interface. Repeating this for all interfaces gives the transmissibility matrix $\mathbf{T}$ for the entire grid.

### 2.4.1 Local flux mimetic multipoint flux approximation

In MRST, the MPFA method is not implemented by using the original MPFA-O formulation, but by using a local-flux mimetic formulation. The following is based on [5, 7, 8, 11]. The inner product matrix $\mathbf{M}$ from the mimetic methods explained in Section 2.3 are symmetric and positive-definite. The inner product matrix $\mathbf{M}$ from this local flux mimetic multipoint flux approximation is block diagonal, but it is not symmetric [5].

We still have our problem:

$$
\begin{aligned}
\vec{f} &= -\mathbf{K}\nabla u, \\
\nabla \cdot \vec{f} &= \frac{q}{\rho}.
\end{aligned}
$$
(2.73)

If we have Dirichlet boundary conditions where $u = 0$ on $\partial\Omega$, then, according to Greens formula, we have:

$$\int_\Omega u(\nabla \cdot \vec{f})dx \;+\; \int_\Omega \nabla u \cdot \vec{f}dx = 0,$$

$$\int_\Omega u(\nabla \cdot \vec{f})dx \;+\; \int_\Omega (-\mathbf{K}^{-1}\vec{f}) \cdot (-\mathbf{K}\nabla u)dx = 0,$$

$$\int_\Omega u(\nabla \cdot \vec{f})dx \;+\; \int_\Omega \mathbf{K}^{-1}\vec{f} \cdot (\mathbf{K}\nabla u)dx = 0. \tag{2.74}$$

The difference between the local-flux mimetic multipoint flux approximation method; (LFMPFA) and the mimetic finite difference method is that for LFMPFA we divide each face into subfaces and then reduce the face centred system to a cell centred system in order to be equivalent to an MPFA method. The elements are as explained in Section 2.3, but now we divide each face $e$ into subfaces $\tilde{e}$. We now want to discretise Equation (2.74).

We have the following scalar products.

**Definition 2.4.1.** *For* $\mathbf{u} = u^I, \mathbf{q} = q^I \in Q^h$:

$$[\mathbf{u}, \mathbf{q}]_{Q^h} = \sum_{E \in \Omega_h} |E| u_E q_E. \tag{2.75}$$

**Definition 2.4.2.** *For* $\mathbf{f} = \vec{f}^I, \mathbf{v} = \vec{v}^I \in X^h$ *we get:*

$$[\mathbf{f}, \mathbf{v}]_{X^h} = \sum_{E \in \Omega_h} \sum_{c \in E} \sum_{s,r=1}^{k_c} (\mathbf{M}_c)_{s,r} f_E^{\tilde{e}_s} v_E^{\tilde{e}_r}, \tag{2.76}$$

*where c is a corner that is shared by different subfaces $\tilde{e}$ of face e of cell E.*

The scalar product defined in Definition 2.4.2 can also be written as:

$$[\mathbf{f}, \mathbf{v}]_{X^h} = \sum_{E \in \Omega_h} [\mathbf{f}, \mathbf{v}]_{X^h, E} = \sum_{E \in \Omega_h} \sum_{c \in E} [\mathbf{f}, \mathbf{v}]_{X^h, E, c}, \tag{2.77}$$

where:

$$[\mathbf{f}, \mathbf{v}]_{X^h, E, c} = \mathbf{M}_c \mathbf{f}_c \cdot \mathbf{v}_c. \tag{2.78}$$

Hence we also have:

$$\begin{aligned}
[\mathbf{f}, \mathbf{v}]_{X^h} &= \sum_{E \in \Omega_h} \sum_{c \in E} \mathbf{v}_c^T \mathbf{M}_c \mathbf{f}_c, \\
&= \sum_{E \in \Omega_h} \mathbf{v}_E^T \mathbf{M}_E \mathbf{f}_E.
\end{aligned} \tag{2.79}$$

We want to approximate Equation (2.74) and we will use the definitions above to show the following proposition.

**Proposition 2.4.2.** *The approximation of Equation* (2.74) *can be written in discretised form as:*

$$\sum_{E\in\Omega_h} |E| u_E (Hf)_E + \sum_{E\in\Omega_h} \sum_{c\in E} \sum_{s,r=1}^{k_c} (\mathbf{M}_c)_{s,r} f_E^{\tilde{e}_s} (Gu)_E^{\tilde{e}_r} = 0. \tag{2.80}$$

*Proof.* We let $\nabla\cdot\vec{f} = Hf$, and we can now approximate the first integral of Equation (2.74):

$$\int_\Omega u(\nabla\cdot\vec{f})d\Omega \approx [\mathbf{u},\mathbf{Hf}]_{Q^h} = \sum_{E\in\Omega_h} |E| u_E (Hf)_E. \tag{2.81}$$

Setting $Gu = \mathbf{K}\nabla u$ the second integral of Equation (2.74) can be approximated by:

$$\int_\Omega \mathbf{K}^{-1}\vec{f}\cdot(Gu)dx \approx [\mathbf{f},\mathbf{Gu}]_{\chi^h} = \sum_{E\in\Omega_h} \sum_{c\in E} \sum_{s,r=1}^{k_c} (\mathbf{M}_c)_{s,r} f_E^{\tilde{e}_s} (Gu)_E^{\tilde{e}_r}. \tag{2.82}$$

Adding these together we get:

$$\sum_{E\in\Omega_h} |E| u_E (Hf)_E + \sum_{E\in\Omega_h} \sum_{c\in E} \sum_{s,r=1}^{k_c} (\mathbf{M}_c)_{s,r} f_E^{\tilde{e}_s} (Gu)_E^{\tilde{e}_r} = 0, \tag{2.83}$$

which is what we wanted to prove.

$\square$

As in Section 2.3 we have a similar expression for the flux:

$$\begin{aligned} f_E^{\tilde{e}} &= -\vec{n}_E^{\tilde{e}}(Gu)_E^{\tilde{e}}, \\ &= -\vec{n}_E^{\tilde{e}}(\mathbf{K}\nabla u)_E^{\tilde{e}}. \end{aligned} \tag{2.84}$$

Similarly to the calculations done in Section 2.3 we get:

$$\begin{aligned} \mathbf{M}_c\mathbf{f} = \mathbf{M}_c\mathbf{N}_c\mathbf{K}\nabla u &= \mathbf{u} - \boldsymbol{\pi} = \mathbf{C}\cdot\nabla u, \\ \mathbf{M}_c\mathbf{N}_c\mathbf{K} &= \mathbf{C}. \end{aligned} \tag{2.85}$$

And hence we get that:

$$\begin{aligned} \mathbf{M}_{Ec} = \mathbf{C}(\mathbf{N}_{Ec}\mathbf{K}_E)^{-1} + \mathbf{M}_{Ec2}, \\ \text{where } \mathbf{M}_{Ec2}\mathbf{N}_{Ec} = 0. \end{aligned} \tag{2.86}$$

24

The matrix $\mathbf{N}_{Ec}$ is consisting of the area-weighted subface normals of the subfaces of cell $E$ connected to a corner $c$. In MRST these subface normals are found by taking the original area-weighted face normals divided by the number of nodes connected to the face, each subface of the face then has this as its normal vector. The permeability tensor $\mathbf{K}_E$ is the permeability for cell $E$. This local-flux mimetic formulation will give the same answer as the MPFA-O method and hence $\mathbf{C}$ contains the original face centroids, not the subface centroids. Note that the matrix $\mathbf{M}_{Ec}$ is computed cell-wise as we consider a cell $E$ and the subfaces of this cell which are connected to corner $c$.

Each cell $E$ has a matrix $\mathbf{M}_E$ which is a block diagonal matrix with as many blocks as there are corners in $E$, i.e., the $\mathbf{M}_{Ec}$ matrices are these blocks. This is done for each cell $E$ and subsequently assembled into the matrix $\mathbf{M}_c$ in such a way that $\mathbf{M}_c$ is a block diagonal matrix having one block for each corner in the entire domain. The size of each block is $n_i \times n_i$, where $n_i$ is the number of subfaces sharing that corner. We then invert this matrix and compute the transmissibility matrix. The transmissibility matrix is reduced by adding the contribution from each subface for all faces.

Note that in `computeMultiPointTrans.m` in MRST, which is the function used to compute the multipoint transmissibilities, the transmissibility matrix $\mathbf{T}$ consists of two parts, these are $\mathbf{T.T}$ and $\mathbf{T.Tg}$. The matrix $\mathbf{T.Tg}$ is required in order to treat gravity correctly.

# Chapter 3

# Monotonicity and cycles

## 3.1 Monotonicity

Different equations satisfy different properties, and when we discretise equations it is often important that these properties are conserved. Elliptic equations satisfy a property called monotonicity, this follows from the maximum principle. Hence, monotonicity is a property which should be conserved when discretising the elliptic equation in Equation (3.1). If this property is not conserved it may lead to extrema in the interior and it may also lead to oscillations [12]. Some discretisation methods i.e., MPFA and MFD violate the monotonicity principle for some cases while TPFA always maintain this property. Whether a method is monotone or not depends on the grid and the properties of the rock [12]. We will in this chapter present the theoretical background for monotonicity.

We have the following elliptic equation for an incompressible fluid:

$$-\nabla \cdot \lambda \nabla u = \frac{q}{\rho}, \tag{3.1}$$

where $\lambda = \frac{\mathbf{K}}{\mu}$ and $u = (p + \rho g z)$.

Let $\Omega$ be our domain, then the solution of Equation (3.1) satisfies the strong maximum principle stated in [13] and [12]:

**Theorem 3.1.1.** (Strong maximum principle) *Assume the permeability tensor* **K** *is continuously differentiable and the domain* $\Omega$ *is connected, open and bounded. If* $q \geq 0$ *in* $\Omega$ *and* $u$ *attains its minimum over* $\overline{\Omega}$ *at an interior point, then* $u$ *is constant within* $\Omega$.

Here, $\overline{\Omega}$ is the domain including $\Omega$ and $\partial\Omega$.

The strong maximum principle depends on Hopf's lemma which according to [12] says that:

**Lemma 3.1.1.** (Hopf's lemma) *Assume that **K** is continuously differentiable and that the boundary is sufficiently smooth. If $q \geq 0$ in $\Omega$, then the solution $u$ of (3.1) has no local minima in $\Omega$. I.e., there is no point $\mathbf{x}_0 \in \Omega$ such that $u(\mathbf{x}_0) < u(\mathbf{x})$ for all other $\mathbf{x}$ in a neighborhood of $\mathbf{x}_0$.*

The above properties hold for the elliptic equation. We now want to find the corresponding discrete properties that need to be fulfilled in order for the discretisation methods to conserve the monotonicity property. Hence we consider Equation (3.1). If we in addition have Dirichlet boundary conditions, $u = 0$ on the boundary $\partial\Omega$, we can write our problem as follows:

$$\begin{cases} -\nabla \cdot \lambda \nabla u = \frac{q}{\rho}, & \text{in } \Omega, \\ u = 0, & \text{on } \partial\Omega. \end{cases} \tag{3.2}$$

As stated in [12] we can use Green's function, $G(\vec{\xi}, \vec{x})$, to express a solution of (3.2).

For a domain $\omega \subset \Omega$

$$u(\vec{x}) = \int_\omega G_\omega(\vec{\xi}, \vec{x}) q(\vec{\xi}) d\tau_\xi. \tag{3.3}$$

The minimum value of $u = 0$, and $q \geq 0$, hence $G_\omega$ must be non-negative everywhere, i.e.,

$$G_\omega \geq 0. \tag{3.4}$$

This must be true for all $\omega \subset \Omega$ in order to guarantee that the solution has no local minima inside $\Omega$.

Generally, a discretisation method will give a set of linear equations:

$$\mathbf{A}\mathbf{u} = \mathbf{q}, \tag{3.5}$$

with the solution

$$\mathbf{u} = \mathbf{A}^{-1}\mathbf{q}. \tag{3.6}$$

Where $\mathbf{A}$ is the discretised operator, $\mathbf{u}$ is the collection of the potential solutions and $\mathbf{q}$ contains the sink/source terms. Now $\mathbf{A}^{-1}$ can be considered as a discrete Green's function and hence we must have:

$$\mathbf{A}^{-1} \geq 0. \tag{3.7}$$

When this is fulfilled, we say that $\mathbf{A}^{-1}$ is monotone, the matrix $\mathbf{A}$ is inverse monotone.

Equation (3.7) excludes negative solutions when we have homogeneous Dirichlet boundary conditions and $\mathbf{q} \geq 0$, but in order to guarantee that the solution has no local minima in $\Omega$, it is required that Equation (3.7) holds for any subset of the grid points that $\mathbf{A}$ is constructed for. This follows directly from the fact that it is a requirement for Green's function [12]. This leads to the discrete maximum principle, [12]:

**Theorem 3.1.2.** (Discrete maximum principle) *For any subgrid $\omega \in \Omega$ with homogeneous Dirichlet boundary conditions which is bounded by a closed Jordan curve, the discretisation must yield a system matrix, $\mathbf{A}$, with a corresponding inverse, $\mathbf{A}^{-1}$, containing no negative elements.*

A Jordan curve, $C$, is a simple closed curve in the plane. The curve $C$ decomposes the plane into two disjoint open connected sets. The common boundary of the sets is the curve $C$ [4].

M-matrices are a special class of inverse monotone matrices. An M-matrix, $\mathbf{A}$, is a nonsingular matrix defined by the following [4]:

$$
\begin{aligned}
a_{i,j} &\leq 0, \text{ for } i \neq j, \\
\mathbf{A}^{-1} &\geq 0.
\end{aligned}
$$

The system matrices obtained by TPFA are M-matrices [12].

In reservoir simulation we have that $\mathbf{f} = \mathbf{Tu}$. We want to discretise Equation (3.2) and here we have that $-\nabla \cdot \lambda \nabla u = \frac{q}{\rho}$ which on matrix form can be written as: $\mathbf{Hf} = \mathbf{q}$ and then we get:

$$
\begin{aligned}
\mathbf{HTu} &= \mathbf{q}, \\
\mathbf{u} &= (\mathbf{HT})^{-1}\mathbf{q},
\end{aligned}
\tag{3.8}
$$

it further follows that $\mathbf{HT}$ is our matrix $\mathbf{A}$.

## 3.2 Cycles in the velocity field

Securing that a specific method is monotone has been an important field of research the last years. Equation (3.1) is a monotonic equation and this is used as a motivation for having discretisation methods preserving this property. When performing reservoir simulations, the system matrix $\mathbf{A}$ becomes very large, and it is therefore not always possible to obtain $\mathbf{A}^{-1}$ to check if the method is monotone. It is difficult to obtain monotone pressure solutions for consistent discretisation methods, and requiring that a method is monotone may sometimes affect the consistency of the method. If we consider a flow consisting of one phase, it is guaranteed that we do not have any

cycles in the flux field [14] if we apply a monotone method. This is one of the most important and beneficial properties of a monotone method.

As before we have our system of equations which consist of:

$$\vec{f} = -\mathbf{K}\nabla u,$$
$$\nabla \cdot \vec{f} = \frac{q}{\rho}, \qquad (3.9)$$

and a transport equation:

$$\frac{\partial(\phi\rho)}{\partial t} + \nabla \cdot (\rho\vec{f}) = q. \qquad (3.10)$$

If a method is not monotone, we may experience false oscillations which can lead to wrong directions of the fluxes resulting in the cycles [12]. A situation with multiphase flow where the pressure solution oscillates, may result in cases where the computed pressure lies below the bubble point pressure while the actual pressure lies above it. If this happens, artificial gas may be liberated resulting in a strongly diverging solution. The flux is a function of the pressure, and oscillations in the pressure may lead to circulations in the flux field, [4]. This is the most important motivation for considering non-physical cycles in the flux field.

The time spent on simulations is an important issue for developing efficient reservoir simulation methods. If we have cycles in the flux, different components are mutually dependent on each other. If we for instance are using an implicit volume method with an upwind discretisation scheme, cycles result in cells being coupled together unnecessarily in the nonlinear system, see e.g., [15]. This will result in matrices with large blocks and the time used to solve the system can be very long. Streamlines can be used to simulate the transport, cycles will, as a worst case scenario, result in streamlines going around in circles, this result in a system that is hard to solve. Therefore, reducing the number and the sizes of the cycles can reduce the running time.

If we consider the graph of directed fluxes, i.e., the cells are vertices and the flux from cell $i$ to cell $j$ is denoted by a directed edge, and if the method is monotone, the resulting graph will be a directed acyclic graph, DAG, since a monotone method results in a field of fluxes containing no cycles. If we have a DAG we can perform a topological sort, see e.g., [16], and reorder our system as explained in [15] resulting in a system where the state of cell $i$ only depends on the state of the previous cells $1, \ldots, i-1$. This will further result in a lower (or upper) triangular system which can be solved much more efficiently than the original system. If we, however, do not have a DAG, we can still group together elements belonging to the same cycles to blocks and solve the system block by block. How fast the system is solved will here depend on the size the largest blocks, i.e., the largest cycles.

A cycle is a class of vertices where all the vertices in the particular class can reach each other [16]. This is also called a strongly connected component.
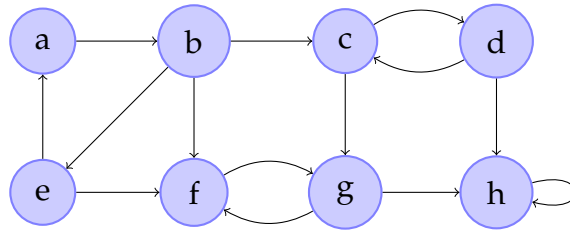
**Figure 3.1:** *Graph with cycles.*

Figure 3.1 shows a directed graph with cycles where the strongly connected components are $a-b-e$, $c-d$, $f-g$ and $h$, while Figure 3.2 shows a directed acyclic graph, DAG.
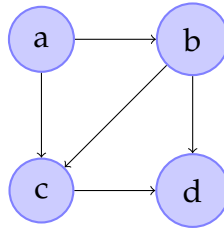


**Figure 3.2:** *Directed acyclic graph.*

Consider Figure 3.3 which is a system consisting of four cells. The arrows represent the direction of the fluxes between the cells, i.e., we have drawn the positive fluxes. We note that we have a cycle.
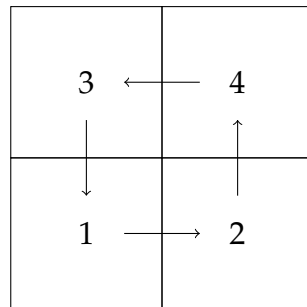


**Figure 3.3:** *Cycle in the velocity field.*

A fluid will flow from high pressure to low pressure, and for the fluxes to have the direction shown in Figure 3.3 we must have that:

$$
\begin{aligned}
u_1 &> u_2, \\
u_2 &> u_4, \\
u_4 &> u_3, \\
u_3 &> u_1.
\end{aligned}
$$

By inserting the second and third equation into the first one, we get that $u_1 > u_3$ which is a violation of the fourth equation which says that $u_3 > u_1$. Having a cycle in the velocity field is therefore not physically correct, for single-phase flow, for models where

the grid cells are quite regular and $\nabla u$ is the gradient pointing from the cell face to the centre of the face. Mathematically this comes from the fact that:

$$\begin{aligned} \vec{f} &= -\mathbf{K}\nabla u, \\ \nabla u \cdot \vec{f} &= -\nabla u \cdot (\mathbf{K}\nabla u). \end{aligned} \quad (3.11)$$

$\mathbf{K}$ is positive definite and hence $\nabla u \cdot (\mathbf{K}\nabla u) > 0$ and this implies that:

$$\nabla u \cdot \vec{f} < 0 \quad \Rightarrow \quad \theta > 90°. \quad (3.12)$$

The results obtained by TPFA will always have the property that the flux goes from the cell with the highest pressure to the cell with the lowest pressure.
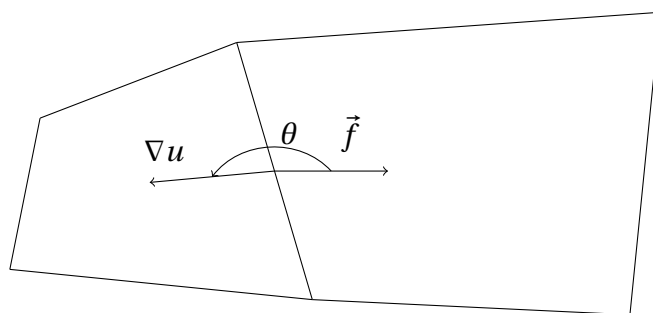


**Figure 3.4:** *Pressure difference and flux direction.*

We have implemented a function which finds out if there are cycles in the flux field, the number of cycles and the size of the cycles. In MRST the fluxes are given in a vector where each row represents a face belonging to two cells, cell $i$ and cell $j$. The function takes as input the grid and the fluxes. The fluxes are then ordered in such a way that if the flux for the face belonging to cell $i$ and $j$ is positive, the value of the flux is placed in a matrix, $\mathbf{B}$ on row $i$, column $j$, and if the flux is negative, it is placed in $\mathbf{B}$ on row $j$, column $i$. We then place ones on the diagonal, and then we use the built-in function in MATLAB, dmperm.

```
[p, q, r] = dmperm(B);
```

This is the same as saying that every cell is in a cycle with itself, but we want the cycles to consist of only one cell. This occurs only during the test as we need to use the function dmperm correctly. The matrix is then interpreted as a directed graph where a non-zero element in $\mathbf{B}_{i,j}$ means that the edge is from vertex $i$ to vertex $j$. The function identifies the strongly connected components. For the graph to be acyclic in reality, i.e., not the modified graph, the number of strongly connected components must be the same as the number of cells, i.e., we want each strongly connected component to only contain one cell.

31

If we do not have any cycles in the flux field, the length of $r$ should be $n + 1$ where $n$ is the number of cells. If we have cycles, the length of $r$ is shorter, and then the number of cycles is $n - 1 - \text{length}(r)$.

# Chapter 4

# Hybrid methods

Different discretisation methods have different advantages and disadvantages. Sometimes it may be beneficial to combine two methods by drawing on the strengths of each method. In the previous chapter we pointed out that TPFA always is monotone and hence the resulting graph of the directed fluxes is always acyclic. We also stated that MPFA and MFD violates the monotonicity principle for some cases and may result in flux-matrices containing nonphysical cycles. We will therefore propose two hybrid methods, the first using a mimetic method in the $xy$-plane and TPFA in the vertical direction, and the second using MPFA in the $xy$-plane and TPFA in the vertical direction. The motivation for doing this is that we believe that using TPFA in the vertical direction will result in hybrid methods with fewer cycles compared to the respective full methods since TPFA contains no cycles. Rather than checking if the hybrid methods presented here are monotone or not, we want to check if the flux field contains cycles or not, and if it contains cycles, we seek to identify the number and sizes of the cycles and compare the results with the respective full methods. The full methods, MPFA and MFD are computationally more costly than TPFA, but in reservoir simulations the grid is constructed in such a way that it coincides with the physical layers in the reservoir. The gridspacing used in reservoir simulations is typically very small in the z-direction compared to the x- and y-direction, [9]. The permeability in the $z$-direction is normally very small compared to the permeability in the $x$- and $y$-direction, and hence most of the flow is along the horisontal layers. It is reasonable to believe that by reducing the number of computations in the $z$-direction and thereby save time we will not reduce the accuracy of the methods too much.

## 4.1 A hybrid mimetic method

We will in this section develop a method applying TPFA in the $z$-direction and a mimetic discretisation in the $xy$-plane.

For each cell in the model we find **C** and **N** as explained in Section 2.3. Furthermore we

need to identify the specific faces which are respectively top faces and bottom faces. For each row in **N** we divide the elements by the area of the respective face. We then identify the faces having the largest $z$-component and the smallest $z$-component, the smallest $z$-component is negative, and this represent the bottom and the top faces of the cell.
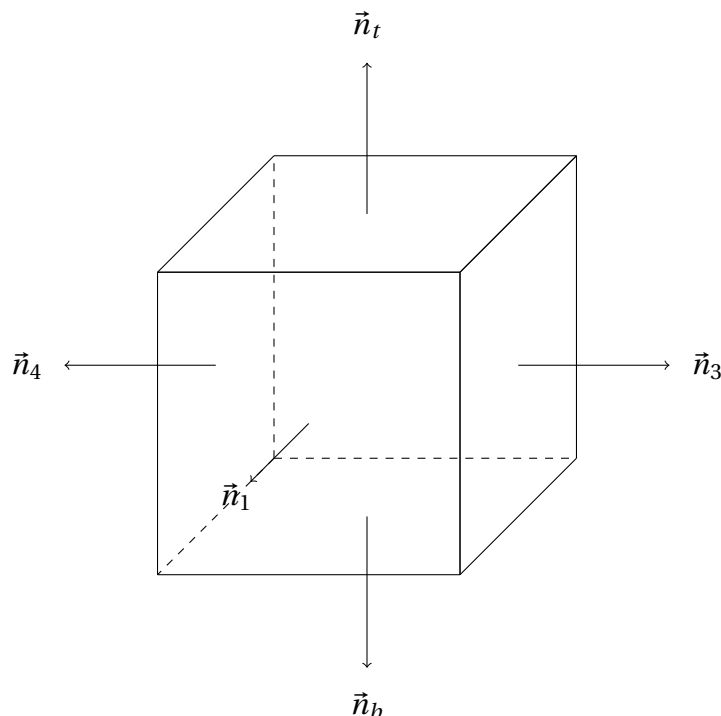


**Figure 4.1:** *One cell with normal vectors.*

We want to project those faces that are not top or bottom down to a plane. This is done by projecting the elements of **C** and **N** belonging to these faces. The elements of **N** for one cell are drawn in Figure 4.1. First, we find an average normal vector which is defined as:

```
average_normal = G.faces.normals(top,:) + G.faces.normals(bottom,:)
```

This is the notation used in MRST where `G.faces.normals(top,:)` is the area weighted normal vector of the top face. These vectors differ from the corresponding vectors in **N** because they are not forced to point out of the respective cell as explained in Section 2.3. Thus, a face may be the top of one cell and the bottom of another cell, but `G.faces.normals` for this face is the exactly the same for both cases while $\vec{n}$ is not.

Second, we find the nullspace of the vector `average_normal` and transpose it, $\mathbf{U} = \text{null(average\_normal)}^{T}$. We project the normal vectors and face centroids of the faces that are not top or bottom down to this.

If $\mathbf{C}_{tmp}$ consists of the face centroids that are not top or bottom, and $\mathbf{N}_{tmp}$ consists of the

area weighted normal vectors for the faces that are not top or bottom, the projection is performed as follows:

$$\mathbf{C}^* = \mathbf{C}_{tmp}\mathbf{U}^\mathbf{T},$$
$$\mathbf{N}^* = \mathbf{N}_{tmp}\mathbf{U}^\mathbf{T}.$$

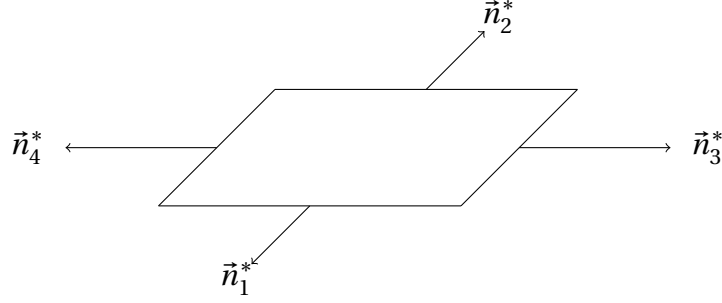The plane and the projected normal vectors are shown in Figure 4.2:



**Figure 4.2:** *Normal vectors projected down to plane.*

The permeability tensor for the xy-plane is: $\mathbf{K}^* = \begin{bmatrix} k_{ii} & k_{ij} \\ k_{ji} & k_{jj} \end{bmatrix}$.

We use the projected normal vectors and face centroids to calculate the mimetic inner product and its inverse in the plane for each cell in our grid:

$$\mathbf{M}^* = \frac{1}{|E_i|}\mathbf{C}^*\mathbf{K}^*\mathbf{C}^{*\mathbf{T}} + \mathbf{Q}_\mathbf{N}^{*\perp}\mathbf{S_M}\mathbf{Q}_\mathbf{N}^{*\perp\mathbf{T}},$$

$$\mathbf{T}^* = \frac{1}{|E_i|}\mathbf{N}^*\mathbf{K}^*\mathbf{N}^{*\mathbf{T}} + \mathbf{Q}_\mathbf{C}^{*\perp}\mathbf{S_T}\mathbf{Q}_\mathbf{C}^{*\perp\mathbf{T}},\tag{4.1}$$

$$\tag{4.2}$$

where $|E_i|$ is the volume of cell $E_i$.

We apply TPFA in the vertical direction, i.e., on the top and bottom faces. The transmissibility matrix for the hybrid multipoint method has diagonal elements in the z-direction, but not in the xy-direction.

We will now develop the actual inner-product and transmissibility being used. In the plane, i.e., on the faces that are not top or bottom, we use the mimetic inner-product in MRST named `ip_simple`, and the inner product will be given by:

$$\begin{aligned}
\mathbf{Q}^* &= \text{orth}(\mathbf{A}^{*-\mathbf{1}}\mathbf{C}^*), \\
\mathbf{M}^* &= \frac{1}{|E_i|}\left(\mathbf{C}^*\mathbf{K}^{*-\mathbf{1}}\mathbf{C}^{*\mathbf{T}} + \frac{\text{diag}|E_i|}{6\text{tr}\mathbf{K}}\mathbf{A}^{*-\mathbf{1}}(\mathbf{I} - \mathbf{Q}^*\mathbf{Q}^{*\mathbf{T}})\mathbf{A}^{*-\mathbf{1}}\right).
\end{aligned}\tag{4.3}$$

And the transmissibility matrix is given by:

$$
\begin{aligned}
\mathbf{Q}^* &= \text{orth}(\mathbf{A}^*\mathbf{C}^*), \\
\mathbf{T}^* &= \frac{1}{|E_i|}\left(\mathbf{N}^*\mathbf{K}^*\mathbf{N}^{*\mathbf{T}} + 6\,tr(\mathbf{K}^*)\mathbf{A}^*(\mathbf{I} - \mathbf{Q}^*\mathbf{Q}^{*\mathbf{T}})\mathbf{A}^*\right),
\end{aligned}
\tag{4.4}
$$

where $\mathbf{A}^*$ is the area of the faces that are not top or bottom, and $\mathbf{C}^*$, $\mathbf{K}^*$ and $\mathbf{N}^*$ are as explained earlier.

In the vertical direction, i.e., on the top and bottom faces TPFA is used. We have used the mimetic formulation of TPFA, i.e., the inner product `ip_tpf` is used:

$$
\begin{aligned}
\mathbf{T} &= \mathbf{NKC^{-1}}, \\
\mathbf{T}_{t,t} &= \vec{n}_t \cdot \mathbf{K}\frac{\vec{c}_t}{|\vec{c}_t|^2}, \\
\mathbf{T}_{b,b} &= \vec{n}_b \cdot \mathbf{K}\frac{\vec{c}_b}{|\vec{c}_b|^2}, \\
\mathbf{M}_{t,t} &= \mathbf{T}_{t,t}^{-1}, \\
\mathbf{M}_{b,b} &= \mathbf{T}_{b,b}^{-1},
\end{aligned}
$$

where $t$ = top and $b$ = bottom.

The matrix is given by:

$$
\mathbf{T} = \begin{bmatrix} \mathbf{T}^* & & \\ & \mathbf{T}_{t,t} & \\ & & \mathbf{T}_{b,b} \end{bmatrix}.
\tag{4.5}
$$

We apply the mimetic formulation of the TPFA method, and this method will be as computationally costly as the mimetic method. We will, however, not pay attention to the time consumed as we are only interested in the numerical values. MRST has a function called `computeMimeticIP.m`, and this contains some mimetic inner products, two of them being `ip_tpf` and `ip_simple`. The hybrid mimetic inner product is added to this function and this inner product will have the same data structure as `ip_tpf` and `ip_simple`. We can therefore use the function in MRST called `solveIncompFlow.m` to solve our system of equations. If we instead had applied the cell centred TPFA formulation, we would have to construct a solver taking into account that part of the matrix needs to be considered as a mimetic system and the other part representing the top and bottom faces of each cell as a system defined by the cell centred TPFA.

## 4.2 Hybrid multipoint method

We have also made a hybrid method using TPFA on the top and bottom faces, i.e., the vertical direction, and MPFA on the other faces, i.e., the plane.
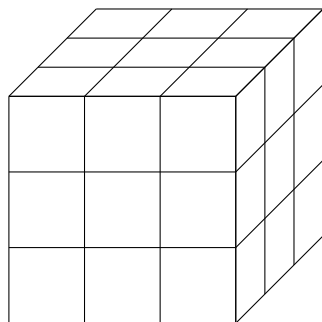


**Figure 4.3:** *Grid with 27 cells.*

Figure 4.3 shows a grid consisting of 27 cells. If we consider the cell in the middle of the grid, Figure 4.4 shows the different planes around this cell, and the faces of this this cell are colored yellow. The black dots are the corners and the dashed lines show the interaction regions. We will use MPFA for the faces that are not top or bottom, and TPFA for the top an bottom faces.
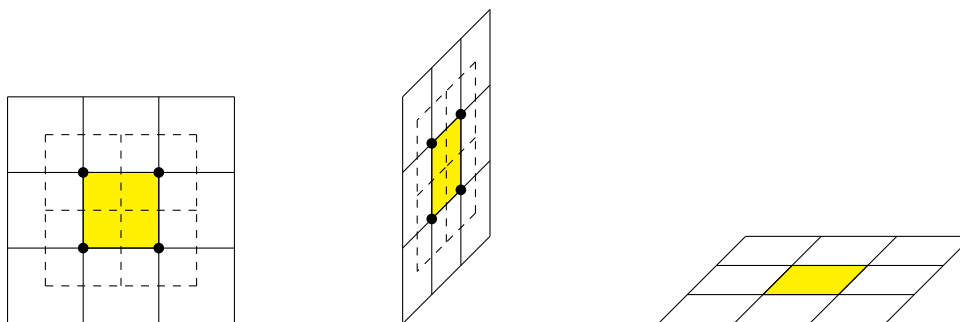


**Figure 4.4:** *Grid in the yz-plane, xz-plane and xy-plane.*

The hybrid MPFA is made by modifying the function in MRST named `computeMultiPointTrans.m`.

Consider the matrix $\mathbf{M}_{Ec}$ as explained at the end of Section 2.4.1. We will also consider the inner product computed by TPFA, $\mathbf{M}_{tpfa}$, this is a diagonal matrix. For all the cells in our domain we detect the subfaces belonging to the top face and the subfaces belonging to the bottom face. We compute $\mathbf{M}_{tpfa}$ for the top, $\mathbf{M}_{tpfa}(top)$ and $\mathbf{M}_{tpfa}(bottom)$ and divide them by the number of nodes making up the different faces, for example:

$$t = \frac{\mathbf{M}_{tpfa}(top)}{\text{Number of nodes on top face}}. \tag{4.6}$$

For the subfaces belonging to this face, we in $\mathbf{M}_{Ec}$ place $t$ on the block diagonal belonging to each of the respective subfaces instead of using the inner product computed by MPFA. For other subfaces not belonging to the top or the bottom face we keep the inner product computed by MPFA. The rest is done in a similar way as for LFMPFA explained in Setion 2.4.1.

Note that for the mimetic hybrid method in Section 4.1 we projected the faces that were not top or bottom down to the $xy$-plane and calculated the mimetic inner product in two dimension for these faces. For the hybrid MPFA method we have, as explained above, replaced the entries of $\mathbf{M}_{Ec}$ belonging to top faces by $t$ and similar for the bottom faces. The entries of $\mathbf{M}_{Ec}$ not belonging to top or bottom faces are kept unchanged, i.e., these are exactly the same as when MPFA is used in the whole domain. Ideally, we should have done a projection of the faces that were not top or bottom down to the $xy$-plane and use MPFA to calculate the $\mathbf{M}$-matrix in two dimensions as we did for the hybrid mimetic method. This would be a very time-consuming task which we did not have the time to do, and hence we chose to implement it as explained earlier in this section. However, this may affect the results for the hybrid MPFA method.

# Chapter 5

# Results

We will in this chapter present the results from testing five different discretisation methods on various cases. We want to compare the exactness of the methods, especially we want to check if the hybrid methods are more exact than TPFA and if they are correct enough compared to the full consistent methods. We have tested the methods by using MRST. We have included most of the test examples in the add-on module `HybridMethods`. The methods we consider are:

1. The two-point flux approximation method, TPFA. In MRST one can use this method as:

```
T = computeTrans(G, rock);
xi = initResSol(G, 0);
Sol = incompTPFA(xi, G, T, fluid, 'bc', bc);
```

2. The mimetic method applying the inner product `ip_simple`, this will be called the mimetic method:

```
T = computeMimeticIP(G, rock, 'InnerProduct', 'ip_simple');
xi = initResSol(G, 0);
Sol = solveIncompFlow(xi, G, T, fluid, 'bc', bc);
```

3. The hybrid mimetic method applying TPFA in the vertical direction and a mimetic method using the inner product `ip_simple` in the plane. We call this the hybrid mimetic method. This is implemented as a new inner product in a function called `computeHybridMimeticIP.m`, the function is added to the add-on module in MRST, `HybridMethods`.

```
T = computeHybridMimeticIP(G, rock, 'InnerProduct', 'ip_hyb');
xi = initResSol(G, 0);
Sol = solveIncompFlow(xi, G, T, fluid, 'bc', bc);
```

4. The local-flux mimetic multipoint flux approximation which we from now on will call MPFA since it gives the same answer as the MPFA-O formulation of the MPFA method.

```
T = computeMultiPointTrans(G, rock);
xi = initResSol(G, 0);
Sol = incompMPFA(xi, G, T, fluid, 'bc', bc);
```

5. The hybrid multipoint method applying TPFA in the vertical direction and MPFA in the plane. We call this the hybrid MPFA. This method is implemented in a new function, `computeHybridMultiPointTrans.m`, as explained in Section 4.2. The function is added to the `HybridMethods` module.

```
T = computeHybridMultiPointTrans(G, rock);
xi = initResSol(G, 0);
Sol = incompMPFA(xi, G, T, fluid, 'bc', bc);
```

We will first consider some basic cases in order to test the accuracy of the hybrid methods. Thereafter we run some more advanced cases to check the nonphysical cycles in the flux field for the different methods. If nothing else is stated, the error is measured as the relative error in the $L^2$ norm.

$$\|u_h - u\|_{L^2} = \left( \frac{1}{V} \sum_i V_i (u_{h,i} - u_i)^2 \right)^{1/2}, \tag{5.1}$$

where $u_h$ is the pressure solution calculated by the respective method, and $u$ is the analytic solution. The relative error is:

$$e_{rel} = \frac{\|u_h - u\|}{\|u\|}. \tag{5.2}$$

When considering the cycles there are a couple of things we want to measure:

1. The number of cells that are in cycles, C, compared to the total number of cells, i.e.,

$$R = \frac{C}{\text{Number of cells}}. \tag{5.3}$$

2. The number of cycles, N.
3. The size of the largest cycle, $n_{max}$.

## 5.1   Regular cartesian grid

We will provide an example showing that for a cartesian grid with homogeneous isotropic permeability $\mathbf{K} = \text{diag}(1,1,1)$ Darcy and linear flow, all five methods provide an accurate answer.

For a cartesian grid, the normal face vectors have the form $\vec{n}_i = c_1 \begin{bmatrix} 1 & 0 & 0 \end{bmatrix}^T$, $\vec{n}_j = c_2 \begin{bmatrix} 0 & 1 & 0 \end{bmatrix}^T$ and $\vec{n}_k = c_3 \begin{bmatrix} 0 & 0 & 1 \end{bmatrix}^T$. When $\mathbf{K} = \text{diag}(1,1,1)$, and by inserting into Equation (2.17) we get:

$$\vec{n}_i \cdot \mathbf{K} \vec{n}_j = c_1 \begin{bmatrix} 1 & 0 & 0 \end{bmatrix} \begin{bmatrix} 1 & 0 & 0 \\ 0 & 1 & 0 \\ 0 & 0 & 1 \end{bmatrix} c_2 \begin{bmatrix} 0 \\ 1 \\ 0 \end{bmatrix} = 0, \tag{5.4}$$

and hence our grid is $\mathbf{K}$-orthogonal.

The grid is a $10 \times 10 \times 5$ grid and the pressure on the global left hand side is 0 while we have imposed a pressure of 100 bar at the global right hand side, i.e., we have linear flow. The pressure solution is shown in Figure 5.1.
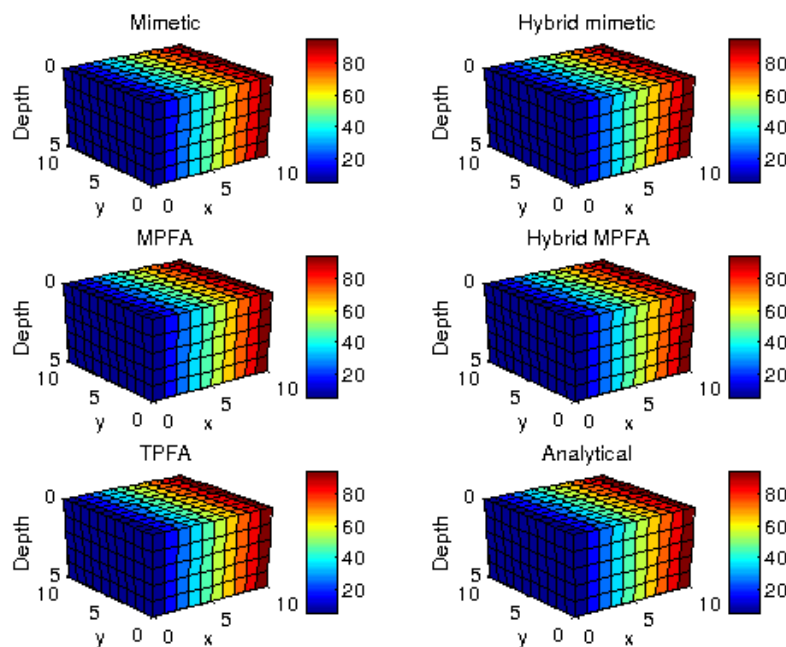


**Figure 5.1:** *Regular cartesian grid.*

We calculated the $L^2$ error, and all methods were exact, as expected. This is due to the fact that all the methods are constructed in such a way that they are exact for linear flow when the grid is $\mathbf{K}$-orthogonal.

## 5.2 Triangle grid

A two-dimensional triangle grid is made and this is extruded to three dimensions. The pillars are vertical. This is done in the following way:

```
nx = 10; ny = 10; nz = 5;
[x,y] = ndgrid(0:nx,0:ny);
G = triangleGrid([x(:) y(:)]);
G = makeLayeredGrid(G, nz);
```

We impose a pressure of 100 bar at the global right hand side of the domain, and the pressure is zero on the left side. The permeability is homogeneous and isotropic, $\mathbf{K} = \mathrm{diag}(1,1,1)$ Darcy.
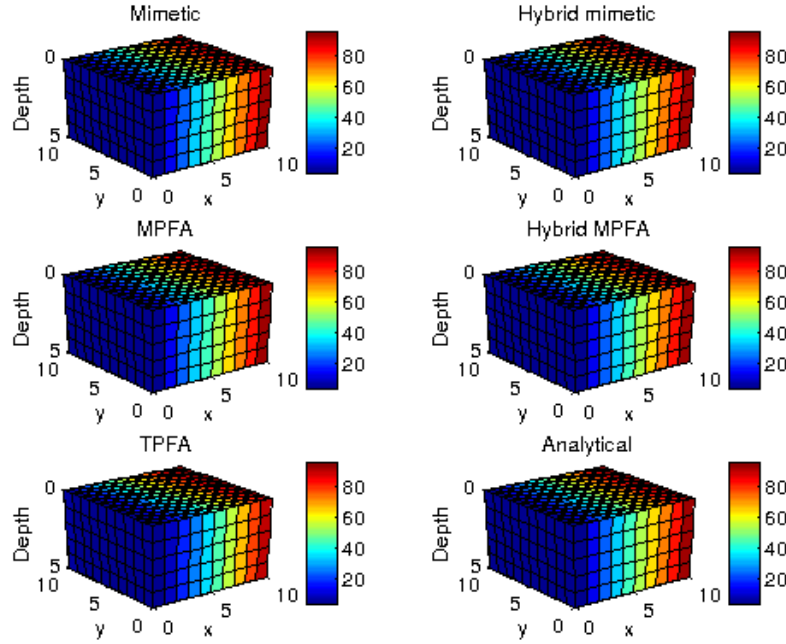


**Figure 5.2:** *Triangle grid with straight vertical pillars.*

Figure 5.2 shows the pressure solutions. The $L^2$ norm of the errors were found and the relative $L^2$ error for TPFA is 0.068174. The other methods give the exact answer.

The mimetic method and MPFA are exact for linear flow even if the grid is not $\mathbf{K}$-orthogonal, and these methods therefore give the exact answer. The flow is in the $x$-direction and the hybrid methods apply the full method in the plane and hence these methods also provide the exact answer.

The cells have a triangular shaped top and bottom and each cell have five faces. Typical normal vectors are on the form $\vec{n}_i = c_1 \begin{bmatrix} 1 & 0 & 0 \end{bmatrix}^T$, $\vec{n}_j = c_2 \begin{bmatrix} 0 & 1 & 0 \end{bmatrix}^T$, $\vec{n}_k = c_3 \begin{bmatrix} 0 & 0 & 1 \end{bmatrix}^T$ and $\vec{n}_l = c_4 \begin{bmatrix} 1 & 1 & 0 \end{bmatrix}^T$. Hence when $\mathbf{K} = \mathrm{diag}(1,1,1)$, and by inserting into Equation (2.17) we get:

$$\vec{n}_i \cdot \mathbf{K}\vec{n}_l = c_1 \begin{bmatrix} 1 & 0 & 0 \end{bmatrix} \begin{bmatrix} 1 & 0 & 0 \\ 0 & 1 & 0 \\ 0 & 0 & 1 \end{bmatrix} c_4 \begin{bmatrix} 1 \\ 1 \\ 0 \end{bmatrix} = 1, \tag{5.5}$$

which shows that the grid cells are not **K**-orthogonal. Due to this, TPFA is not exact.

## 5.3 Perpendicular bisector grid

A 2.5D perpendicular bisector (PEBI) grid is made. The construction of the grid is explained in [17]. First we generate a set of points, and second we triangulate the set of points by using the function `triangleGrid`, as explained in Section 5.2, and thereafter we construct a PEBI grid using the function `pebi`. This is a two dimensional grid and by vertical pillars in the z-direction we extrude it to three dimensions using the function `makeLayeredGrid`.

A linear pressure field is made. The pressure is zero on the global left boundary, and 100 bar at the global right boundary. The permeability is set to be **K** = diag(1, 1, 1) in all of the cells.
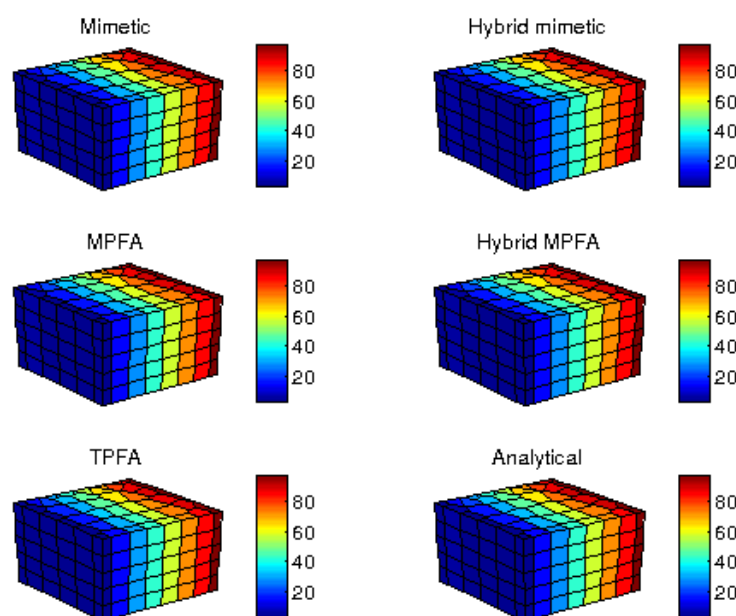


**Figure 5.3:** *Pressure profile, linear flow for PEBI-grid.*

Figure 5.3 shows the pressure profile using TPFA, the mimetic method, the hybrid mimetic method, MPFA, hybrid MPFA and the analytical solution. All profiles look the same, but the relative $L^2$ error is calculated and it is 0.009347 for TPFA. The top and bottom faces of each cell are parallel, they have the same size and they do not vary in the z-direction, as for the triangular grid in Section 5.2. This is a type of grid where the mimetic, MPFA and the hybrid methods should give exactly similar answers, and these answers should be equal to the analytical solution. We find this to be correct. This is caused by the fact that the top and bottom faces of each cell are parallel, and

hence, it is sufficient to use TPFA in the vertical direction. In the $xy$-plane the cells are not **K**-orthogonal, but the mimetic method and MPFA are exact for linear flow even if the grid is not **K**-orthogonal. We note that TPFA gives a small error, as expected since the grid is not **K**-orthogonal.

## 5.4   Twisted grid with increasing slope

We have a grid which is twisted in the $xy$-plane. The grid has $10 \times 5 \times 5$ grid blocks and the physical dimensions are $1000 \times 500 \times 20$. The angle, $\theta$, between the grid and the principal $x$-axis is increased, but the top and bottom faces are always parallel. The permeability is diagonal and anisotropic where the rate, $r = \frac{\text{permX}}{\text{permZ}}$ and permX = permY. The numbers presented in Tables 5.1, 5.2, 5.3, 5.4, 5.6 and 5.7 are the sum of the absolute values of the flux on the boundary. We believe that the cycles occur if we have grids with high anisotropic permeability and if the angle between the grid and the $xy$-plane is relatively large. We seek to find if we can avoid nonphysical cycles in the flux field if the hybrid methods are used instead of the full methods.
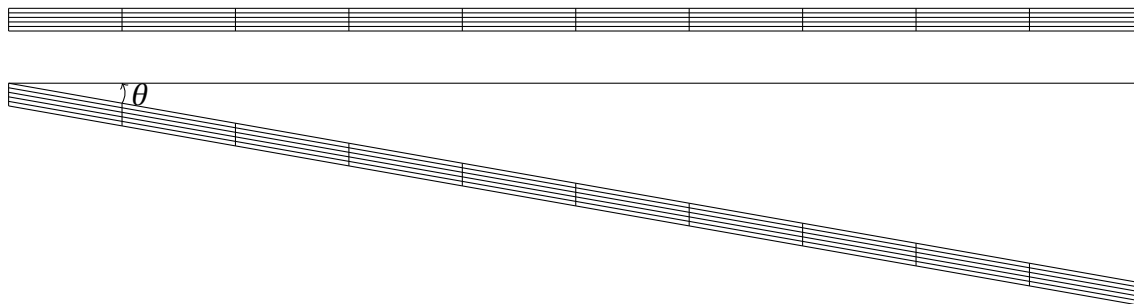


**Figure 5.4:** *The grid when $\theta = 0°$ and $\theta = 10°$.*

Figure 5.4 shows the grid if there is no slope and if the slope is $10°$.

The original permeability is **K** $=$diag(1,1,1) Darcy, but the $z$-component of the permeability is changed according to $r$. We have imposed a pressure of 100 bar at the right hand side of the grid while we have zero pressure on the left hand side of the grid.

Table 5.1 shows the flux-values for the different cases when TPFA is used. We note that the value of the flux is not affected by the anisotropic rate, but it changes slightly according to the slope of the grid. None of the cases include cycles as expected since TPFA is always monotone.

When using the hybrid mimetic method we ran the example twice with different approximations of the permeability in the plane.

The first time we used the hybrid mimetic method, we used a projection of the permeability, i.e., $\mathbf{K}^* = \mathbf{K}\mathbf{U}\mathbf{K}^T$, where **U** is as explained in Section 4.1. The result is shown in Table 5.2. These flux values are similar to the TPFA flux values. We do not get any cycles, this is as we hoped for. However, when $\theta \geq 2$ we can see that for a constant $\theta$, the total flux changes, this does not happen for TPFA. This comes from the

**Table 5.1:** *Flux values calculated by TPFA at the left boundary, where r = permX/permZ and θ is the angle between the grid and the xy-plane.*

| r | θ | | | | |
|---|---|---|---|---|---|
|   | 0 | 1 | 2 | 5 | 10 |
| 1 | 0.0981 | 0.0980 | 0.0979 | 0.0973 | 0.0951 |
| 2 | 0.0981 | 0.0980 | 0.0979 | 0.0973 | 0.0951 |
| 5 | 0.0981 | 0.0980 | 0.0979 | 0.0973 | 0.0951 |
| 10 | 0.0981 | 0.0980 | 0.0979 | 0.0973 | 0.0951 |
| 100 | 0.0981 | 0.0980 | 0.0979 | 0.0973 | 0.0951 |
| 1000 | 0.0981 | 0.0980 | 0.0979 | 0.0973 | 0.0951 |
| inf | 0.0981 | 0.0980 | 0.0979 | 0.0973 | 0.0951 |

fact that we projected the permeability down to the $xy$-plane. When $\theta$ is increased the $z$-component of the normal vector for the top and bottom faces is decreased while the $x$-component is increased. Because of this, the $x$-component of **U** is decreased by a factor $\epsilon_x$, and the $z$-component of **U** is increased by a factor $\epsilon_z$. When the permeability is projected, the change in the permeability in the $x$-direction compared to the original one will be $\epsilon_z \text{permZ} - \epsilon_x \text{permX}$. This is the reason why the flux values changes when the permeability in the $z$-direction changes, even if the angle is kept constant. This can clearly be seen when $\theta \geq 5$, when $\theta$ is smaller than this, $\epsilon_x$ and $\epsilon_z$ are quite small.

**Table 5.2:** *Flux values calculated by the hybrid mimetic method at the left boundary, where r = permX/permZ and θ is the angle between the grid and the xy-plane. The permeability in the plane is made by a projection of the original permeability.*

| r | θ | | | | |
|---|---|---|---|---|---|
|   | 0 | 1 | 2 | 5 | 10 |
| 1 | 0.0982 | 0.0982 | 0.0981 | 0.0975 | 0.0953 |
| 2 | 0.0982 | 0.0982 | 0.0980 | 0.0971 | 0.0938 |
| 5 | 0.0982 | 0.0982 | 0.0980 | 0.0969 | 0.0930 |
| 10 | 0.0982 | 0.0982 | 0.0980 | 0.0968 | 0.0927 |
| 100 | 0.0982 | 0.0982 | 0.0980 | 0.0967 | 0.0924 |
| 1000 | 0.0982 | 0.0982 | 0.0980 | 0.0967 | 0.0924 |
| inf | 0.0982 | 0.0982 | 0.0980 | 0.0967 | 0.0924 |

The second time we used the hybrid mimetic method we chose the permeability to be: $\mathbf{K}^* = \text{diag}(1, 1)$ Darcy, and hence the permeability in the plane will be the same for all cases, and it will not be affected by the change of the permeability in the $z$-direction. Because of this, the calculated flux will not be affected by the change of the permeability in the $z$-direction, it will only be affected by the angle $\theta$. This is shown in Table 5.3. The values are similar to those obtained by TPFA, and, as TPFA, they do not vary according to the anisotropic rate.

The red cells in Table 5.4 include the cases with cycles in the flux field. We can see that this occurs for the first time when $r = 1000$ for the case when $\theta = 10°$. When $r = \text{inf}$ and $\theta > 0$ we see that the flux values are very small, we can also see that the

**Table 5.3:** *Flux values calculated by the hybrid mimetic method at the left boundary, where r = permX/permZ and θ is the angle between the grid and the xy-plane. The permeability in the plane is set to be $\mathbf{K}^* = diag(1,1)$ Darcy.*

| r | θ | | | | |
|---|--------|--------|--------|--------|--------|
|   | 0 | 1 | 2 | 5 | 10 |
| 1 | 0.0982 | 0.0982 | 0.0981 | 0.0975 | 0.0953 |
| 2 | 0.0982 | 0.0982 | 0.0981 | 0.0975 | 0.0953 |
| 5 | 0.0982 | 0.0982 | 0.0981 | 0.0975 | 0.0953 |
| 10 | 0.0982 | 0.0982 | 0.0981 | 0.0975 | 0.0953 |
| 100 | 0.0982 | 0.0982 | 0.0981 | 0.0975 | 0.0953 |
| 1000 | 0.0982 | 0.0982 | 0.0981 | 0.0975 | 0.0953 |
| inf | 0.0982 | 0.0982 | 0.0981 | 0.0975 | 0.0953 |

flux values changes even if θ is constant. The reason for this is that the mimetic inner product is designed in such a way that when the grid is not **K**-orthogonal, the flux in one direction will be affected by the permeability in other directions, as explained for the hybrid mimetic method when the projected permeability was used. This is done such that the mimetic method is exact when we have linear flow, even if the grid is not **K**-orthogonal, but as seen here, this can cause difficulties when the anisotropic rate is very large.

**Table 5.4:** *Flux values calculated by the mimetic method at the left boundary, where r = permX/permZ and θ is the angle between the grid and the xy-plane. The red cells represent the cases where we have cycles.*

| r | θ | | | | |
|---|--------|--------|--------|--------|--------|
|   | 0 | 1 | 2 | 5 | 10 |
| 1 | 0.0982 | 0.0982 | 0.0981 | 0.0975 | 0.0953 |
| 2 | 0.0982 | 0.0982 | 0.0980 | 0.0968 | 0.0925 |
| 5 | 0.0982 | 0.0981 | 0.0976 | 0.0946 | 0.0851 |
| 10 | 0.0982 | 0.0979 | 0.0971 | 0.0914 | 0.0753 |
| 100 | 0.0982 | 0.0956 | 0.0884 | 0.0575 | 0.0249 |
| 1000 | 0.0982 | 0.0810 | 0.0513 | 0.0130 | 0.0035 |
| inf | 0.0982 | $2.1931 \cdot 10^{-12}$ | $4.9755 \cdot 10^{-13}$ | $3.7703 \cdot 10^{-13}$ | $6.0588 \cdot 10^{-13}$ |

Table 5.5 shows the ratio of cells in cycles, the number of cycles and the size of the largest cycle for the cases with cycles for the mimetic method. We note that there are few cycles, but they are quite large. When r = inf and θ = 10 there is only one cycle, but the size of this cycle is 248, i.e., there are only two cells in the entire domain that are not in this cycle.

For the hybrid MPFA method we have no cycles in the flux field. However, the values of the flux when r = inf and θ > 0 are very small. In Chapter 4 we explained how the hybrid methods were implemented. The hybrid mimetic method is made by projecting the faces that are not top or bottom to the xy-plane and applying the mimetic inner product here. The hybrid MPFA method is made by calculating the

**Table 5.5:** *Dimensions of the cycles for the mimetic method, where r = permX/permZ and θ is the angle between the grid and the xy-plane.*

| r | θ | R | N | $n_{max}$ |
|---|---|---|---|---|
| 1000 | 10 | 0.5920 | 2 | 74 |
| inf | 1 | 0.8240 | 1 | 206 |
| inf | 2 | 0.9000 | 1 | 225 |
| inf | 5 | 0.9360 | 2 | 231 |
| inf | 10 | 0.9920 | 1 | 248 |

MPFA transmissibilities and then replacing the entries that belongs to top or bottom with the TPFA transmissibilities. Ideally we should have done a projection for the hybrid MPFA method as well. We believe that not doing this is affecting our results in a bad way, and may part of the reason why we get very small flux values when the anisotropic rate is high, and causing large differences in the flux-values even if θ is constant.

**Table 5.6:** *Flux values calculated by the hybrid MPFA method at the left boundary, where r = permX/permZ and θ is the angle between the grid and the xy-plane.*

| r | θ | | | | |
|---|---|---|---|---|---|
| | 0 | 1 | 2 | 5 | 10 |
| 1 | 0.0982 | 0.0982 | 0.0981 | 0.0975 | 0.0953 |
| 2 | 0.0982 | 0.0982 | 0.0980 | 0.0967 | 0.0925 |
| 5 | 0.0982 | 0.0981 | 0.0976 | 0.0946 | 0.0850 |
| 10 | 0.0982 | 0.0979 | 0.0970 | 0.0913 | 0.0750 |
| 100 | 0.0982 | 0.0953 | 0.0876 | 0.0557 | 0.0240 |
| 1000 | 0.0982 | 0.0754 | 0.0444 | 0.0114 | 0.0031 |
| inf | 0.0982 | $3.2315 \cdot 10^{-13}$ | $8.0877 \cdot 10^{-14}$ | $1.2790 \cdot 10^{-14}$ | $2.9592 \cdot 10^{-15}$ |

For MPFA we have cycles when r = inf and θ > 0, and for these cases we also have very small flux-values. The values are shown in Table 5.7.

**Table 5.7:** *Flux values calculated by MPFA at the left boundary, where r = permX/permZ and θ is the angle between the grid and the xy-plane. The red cells represent the cases where we had cycles.*

| r | θ | | | | |
|---|---|---|---|---|---|
| | 0 | 1 | 2 | 5 | 10 |
| 1 | 0.0982 | 0.0982 | 0.0981 | 0.0975 | 0.0953 |
| 2 | 0.0982 | 0.0982 | 0.0980 | 0.0967 | 0.0925 |
| 5 | 0.0982 | 0.0981 | 0.0976 | 0.0946 | 0.0851 |
| 10 | 0.0982 | 0.0979 | 0.0970 | 0.0913 | 0.0752 |
| 100 | 0.0982 | 0.0955 | 0.0883 | 0.0572 | 0.0247 |
| 1000 | 0.0982 | 0.0806 | 0.0507 | 0.0131 | 0.0034 |
| inf | 0.0982 | $2.1045 \cdot 10^{-12}$ | $1.5612 \cdot 10^{-13}$ | $1.7577 \cdot 10^{-14}$ | $1.7345 \cdot 10^{-14}$ |

In Table 5.8 we see that when cycles occur, there are many cells that are in cycles. As for the mimetic method, we have few cycles, but they are very large. When $r = $ inf and $\theta = 5$, $\theta = 10$ there are only two and three cells that are not in a cycle.

**Table 5.8:** *Dimensions of the cycles for MPFA, where r = permXpermZ and $\theta$ is the angle between the grid and the xy-plane.*

| r | $\theta$ | R | N | $n_{max}$ |
|-----|----|--------|---|-----|
| inf | 1 | 0.7920 | 2 | 99 |
| inf | 2 | 0.4720 | 2 | 59 |
| inf | 5 | 0.9920 | 1 | 248 |
| inf | 10 | 0.9880 | 1 | 247 |

The results obtained in this section has shown us that when we have a very large anisotropic permeability rate and a grid with an angle between the grid and the principal $xy$-plane that is larger than zero, then using a hybrid method instead of a full consistent method will result in a flux field with no cycles. Note that the angle between the grid and the $xy$-plane does not need to be large before cycles in the flux field occur if we have a very high anisotropic permeability, they occur already when $\theta = 1°$. We can also see that there are no cycles when the grid is parallel to the $xy$-plane, but for this case, the grid is actually **K**-orthogonal. It is also worth noting that we need a very high anisotropic permeability before the cycles occur for the full consistent methods. For the mimetic method, $r$ must be inf, i.e., permZ $\approx 0$ before we experience any cycles, while for MPFA, $r = 1000$, but then we must have $\theta = 10°$. The hybrid methods and TPFA provide results containing no cycles.

## 5.5 Grid with skew pillars

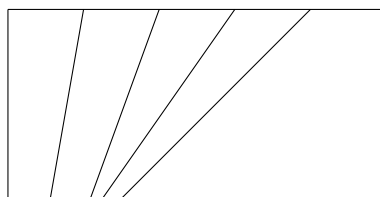A grid with skew pillars is made. The skewed pillars have a slope of 10°, 20°, 35° and 45° respectively.



**Figure 5.5:** *Skewed pillars.*

The grid is a $5 \times 1 \times 5$ grid where the physical dimensions are $50 \times 1 \times 25$ to start with. The angles are kept constant while the length in the $x$-direction is changed so that the ratio $Dx/Dz$ changes, $Dx$ and $Dz$ are the physical dimensions. The permeability is set to be **K** $= \text{diag}(1, 1, 1)$ Darcy and we have imposed a linear pressure field on the model. The numbers presented in Table 5.9 are total flux values on the global right hand side.

**Table 5.9:** *Total flux calculated at the left boundary by the different methods, where Dx and Dz is the physical dimensions in the x- and z-direction.*

| Method | $Dx/Dz$ | | | | |
|---|---|---|---|---|---|
| | 2 | 5 | 10 | 50 | 100 |
| TPFA | 0.1540 | 0.0598 | 0.0297 | 0.0059 | 0.0030 |
| Hybrid mimetic | 0.1546 | 0.0599 | 0.0297 | 0.0059 | 0.0030 |
| Mimetic | 0.1480 | 0.0592 | 0.0296 | 0.0059 | 0.0030 |
| Hybrid MPFA | 0.1536 | 0.0598 | 0.0297 | 0.0059 | 0.0030 |
| MPFA | 0.1480 | 0.0592 | 0.0296 | 0.0059 | 0.0030 |
| Analytic solution | 0.1480 | 0.0592 | 0.0296 | 0.0059 | 0.0030 |

The mimetic method and MPFA give the same answer as the analytic solution for all ratios, this was as expected since we have linear flow. The hybrid methods and TPFA provide the same answer as the analytic solution when $Dx/Dz = 50$, and almost the same when $Dx/Dz = 10$. We note that when the ratio $Dx/Dz$ is large enough, the answer is reasonable accurate when we apply TPFA in the $z$-direction and the mimetic method or MPFA in the $xy$-plane, in fact one actually get a good enough answer by using TPFA in the entire domain. I.e., for grids where the faces are flat and the ratio $Dx/Dz$ is large enough, it is sufficient to use the hybrid methods, even if the pillars are skew.

## 5.6 One-layered real-field model

We now consider one layer of a real-field model. This model is also discussed in [5] where TPFA and the mimetic `ip_qrt` are compared. The model is provided by SIN-TEF. The model is a synthetic model derived from the first layer of a 3D simulation model of a Norwegian offshore reservoir. The layer is flattened and modified in such a way that the corner-point pillars are vertical and the thickness is constant. There is one perforation for each of the original wells. Each well has a rate $q_i$ and is situated at $(x_i, y_i)$. The wells are modelled as logarithmic singularities along the vertical lines at $(x_i, y_i)$. For an infinite domain with constant permeability, the analytic solution of the pressure can, according to [5], be written as:

$$p(x, y, z) = \sum_{i=1}^{n} \frac{q_i}{2\pi \mathbf{K}} \ln \left( \sqrt{(x - x_i)^2 + (y - y_i)^2} \right). \tag{5.6}$$

We have used the five methods discussed earlier to calculate the solution, and the results are shown in Figure 5.6.

As we can see, the solutions look quite similar. We have compared the solutions to the analytical solution and plots of the errors for all the cells are shown in Figure 5.7. TPFA provides a solution with a larger error than the other methods. Note that the span of the colorbar is larger for TPFA compared to the other methods. For the other
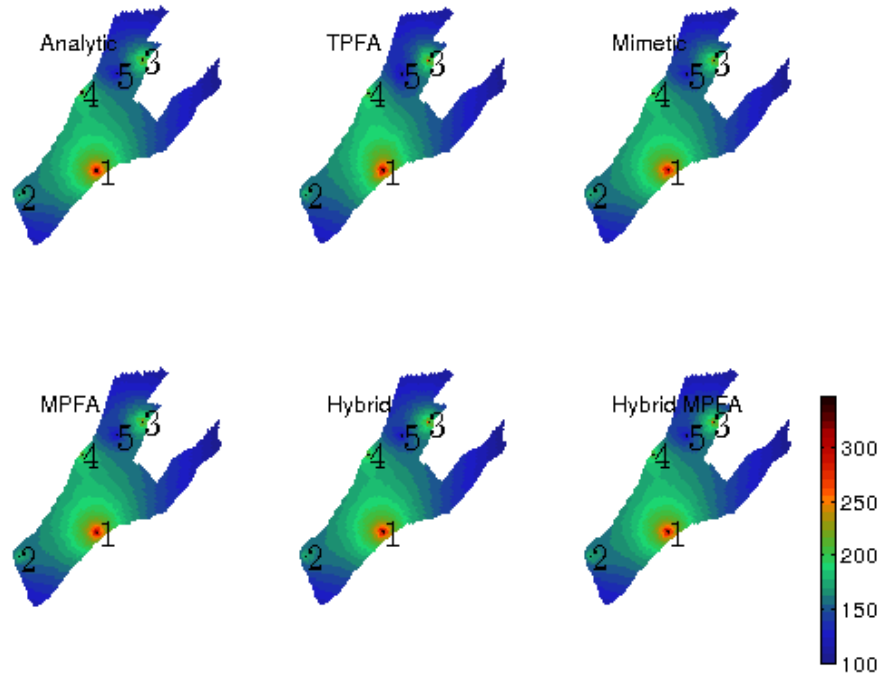
**Figure 5.6:** *Solution of the pressure for a real-field model*

methods the errors occur very close to the wells, while for TPFA the largest errors are also situated close to the wells, but we have a much larger area where the solution is not exactly correct.

The maximum error is then calculated. The pressure in the well cells are defined such that the analytic solution in the well cells is infinite, and we therefore do not calculate the errors in those cells. The maximum discrepancy between the analytic pressure solution and the numerical solutions is calculated, and the discrepancy is then scaled by the span of the analytic pressure solution. The results are shown in Table 5.10

**Table 5.10:** *Maximum error for the different methods.*

| Method | Error |
|---|---|
| TPFA | 0.056021 |
| Hybrid mimetic | 0.009667 |
| Mimetic | 0.010209 |
| Hybrid MPFA | 0.015073 |
| MPFA | 0.015756 |

The maximum error for TPFA is approximately five times as large as the maximum error for the other methods. The maximum errors for the other methods are quite similar, but note that the errors for the hybrid methods are slightly smaller than the errors for their respective full methods.
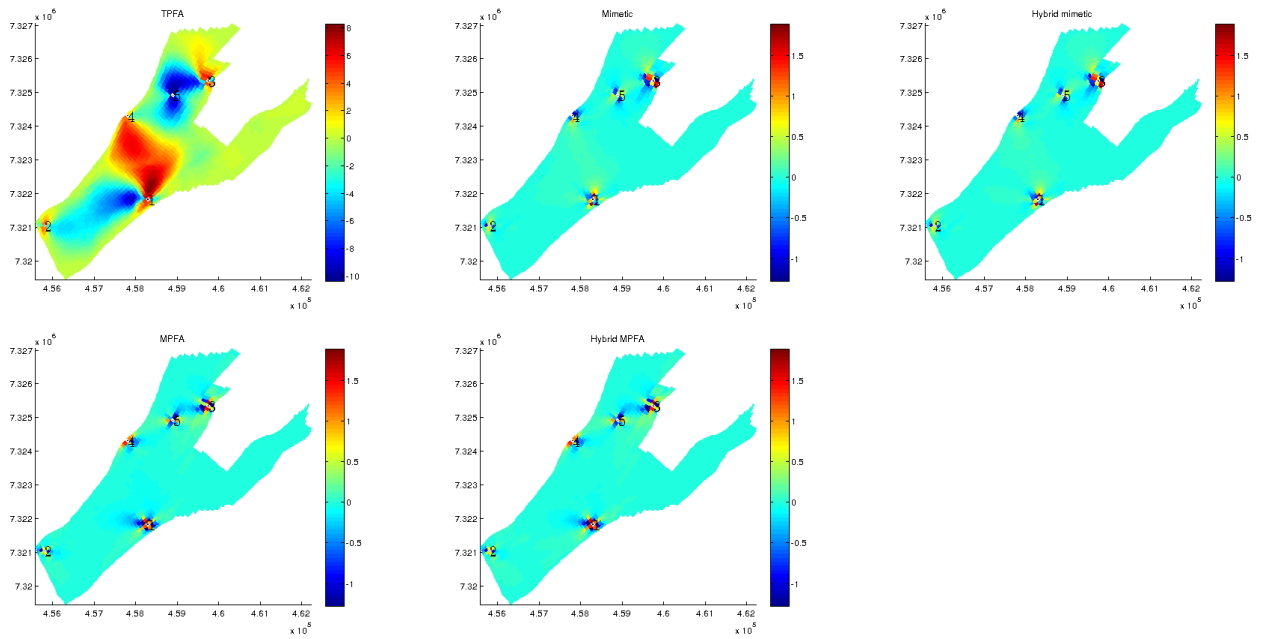
50

**Figure 5.7:** *Plot of the error. On the first row: TPFA, the mimetic method and the hybrid mimetic method. On the second row: MPFA and the hybrid mimetic method.*

The model is as explained earlier one layer of the real field model which is flattened and modified such that the thickness of the layer is constant. These properties make the grid ideal for the hybrid methods since these methods are consistent in the plane. In the vertical direction the methods apply TPFA, but the top and bottom faces are parallel, and in addition, the sizes of the grid blocks in the *x*- and *y*-direction are much larger than in the *z*-direction. This case is thus ideal for the hybrid methods, and as expected, the hybrid methods provide reasonable accurate answers.

## 5.7 Pebi grid containing a curved fault

We will in this section consider a 2.5D PEBI grid containing a curved fault. The grid is the same as explained in Example 6 in [5]. We impose a pressure difference on the grid, where the pressure is 250 bar on the global west side of the reservoir, and 100 on the global east side. The grid is shown in Figure 5.8.

### 5.7.1 Homogeneous isotropic permeability

We begin with a permeability $\mathbf{K} = \text{diag}(1,1,1)$ Darcy in all of the cells and the porosity $\phi = 0.3$. We want to compare the different methods in relation to the number of cycles. The methods considered are the mimetic method, the hybrid mimetic method, MPFA and the hybrid MPFA.

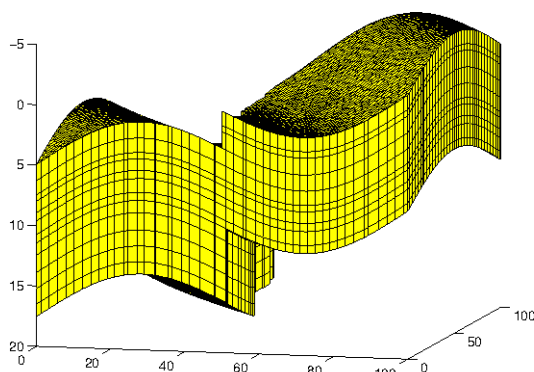We note that both hybrid methods provide solutions without cycles while the full

**Figure 5.8:** *2.5D PEBI grid containing a curved fault.*

**Table 5.11:** *Results concerning cycles for the flux field with homogeneous isotropic permeability. R is the ratio of cells in cycles, N is the number of cycles and $n_{m}ax$ is the size of the largest cycle.*

| Method | R | N | $n_{max}$ |
|---|---|---|---|
| Hybrid mimetic | 0 | 0 | 0 |
| Mimetic | 0.0003 | 1 | 7 |
| Hybrid MPFA | 0 | 0 | 0 |
| MPFA | 0.0054 | 2 | 119 |

methods have flux solutions with nonphysical cycles. We had isotropic permeability and a linear pressure drop, and originally we believed that neither of the methods would provide results with cycles in the flux field. In Section 5.4 we did not get cycles for any of the methods when the permeability was isotropic even if the grid was not parallel to the $xy$-plane. The reason for the cycles in the full consistent methods must come from the fact that there is a curved fault in the grid. However the cycles are few, only one for the mimetic case and two for MPFA. We also see that MPFA has a larger maximum cycle and the number of cells in cycles is larger than for the mimetic method.

## 5.7.2 Homogeneous anisotropic permeability

We will now consider the same grid, but the permeability is set to be $\mathbf{K} = \mathrm{diag}(1, 1, 0.01)$ Darcy in all of the grid cells.

Figure 5.9 shows the pressure solutions from the mimetic method, the hybrid mimetic method, MPFA and the hybrid MPFA method. We see that they do not give exactly similar answers. We have also compared the number of cycles in the flux field for the different methods.

From Table 5.12 we note that the hybrid methods are still free of cycles even if we have anisotropic permeability. The mimetic method and MPFA give large cycles, and
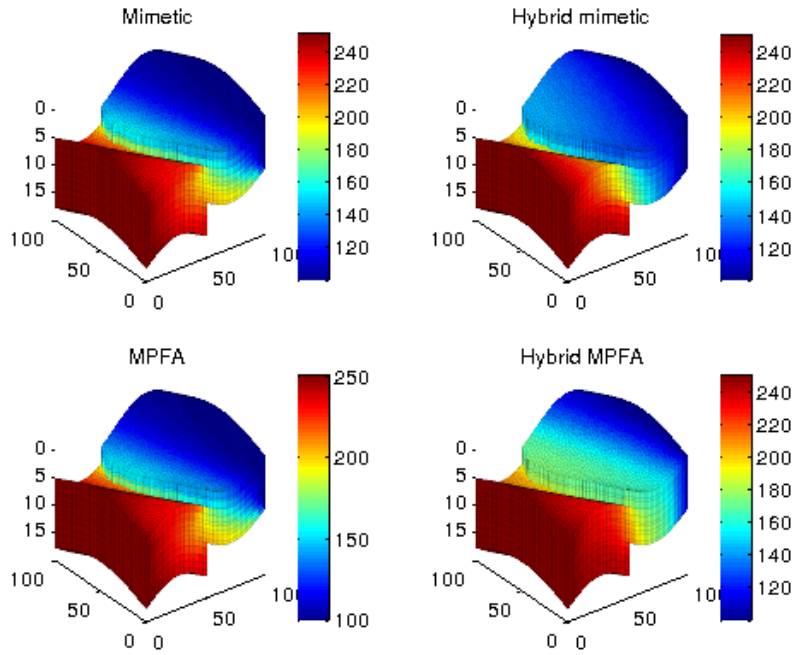
**Figure 5.9:** *Pressure solution with anisotropic permeability*

**Table 5.12:** *Results concerning cycles for the flux field with homogeneous anisotropic permeability R is the ratio of cells in cycles, N is the number of cycles and $n_m ax$ is the size of the largest cycle.*

| Method | R | N | $n_{max}$ |
|---|---|---|---|
| Hybrid using ip_simple | 0 | 0 | 0 |
| Mimetic | 0.1090 | 69 | 611 |
| Hybrid MPFA | 0 | 0 | 0 |
| MPFA | 0.0864 | 45 | 567 |

they give more cycles than when the permeability was isotropic. We have permuted the flux-matrices using `dmperm`. If the flux field is free of cycles we will get an upper triangular matrix, but if it is not free of cycles we will get elements below the diagonal. Figure 5.10 shows the permuted flux-matrices obtained by the mimetic method and MPFA where the cycles are drawn. The sizes of the squares are the same sizes as the cycles and we can see that the structures of the matrices are quite similar.

It is not easy to see that the matrices are not upper triangular and hence we have plotted the elements that are under the diagonal in Figure 5.11.

We thought that the full consistent methods would have cycles since we have a grid where the top and bottom faces are not parallel to the $xy$-plane and we have anisotropic permeability with an anisotropic rate of 100. We believed that the hybrid methods would turn out to be free of cycles since they use TPFA in the vertical direction hence this was as expected.
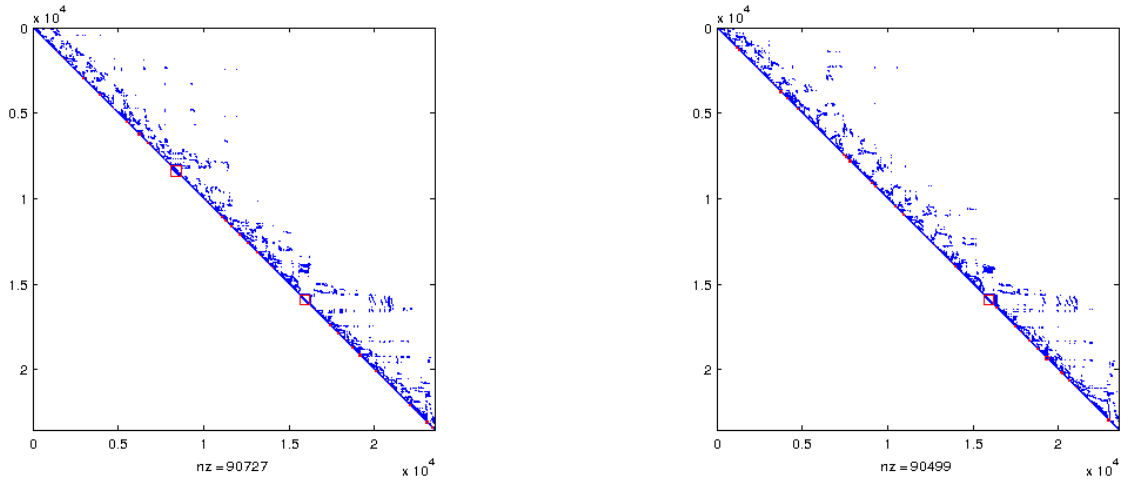
**Figure 5.10:** *The perturbed flux-matrix with cycles for the mimetic method to the left and for MPFA to the right.*
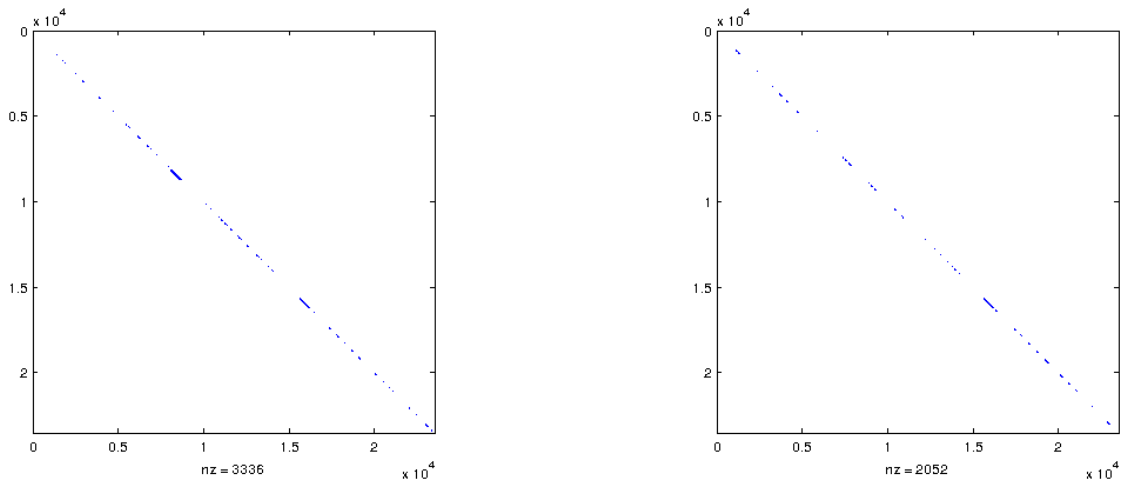


**Figure 5.11:** *The elements under the diagonal for mimetic to the left and MPFA to the right.*

## 5.8 Considering cycles of a real field model

We will in this section discuss the results in relation to cycles by using TPFA, the mimetic method and the hybrid mimetic method on a real field model. We do not consider MPFA and the hybrid MPFA as these are not fully applicable to this model. The model is shown in Figure 5.12.

The dimension of the cells in the model is typical for a model used in reservoir simulation. The cells have a much larger extent in the *x*- and *y*-direction compared to the extent in the vertical direction. We place six wells in the model, three are injection wells and three are production wells. The wells are controlled by a bottom hole pressure of 300 bar for the injection wells and 100 bar for the production wells. The placement of the wells are shown in Figure 5.13.
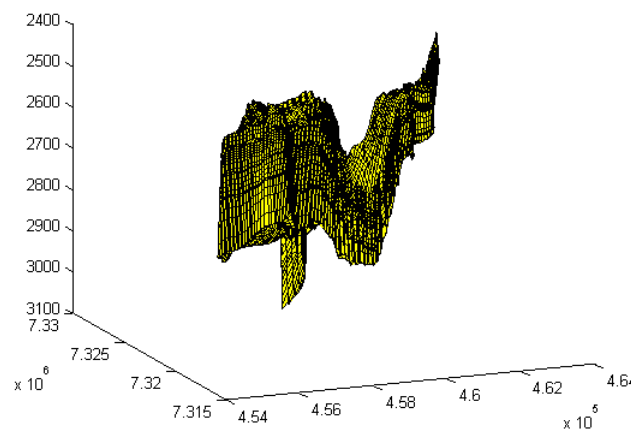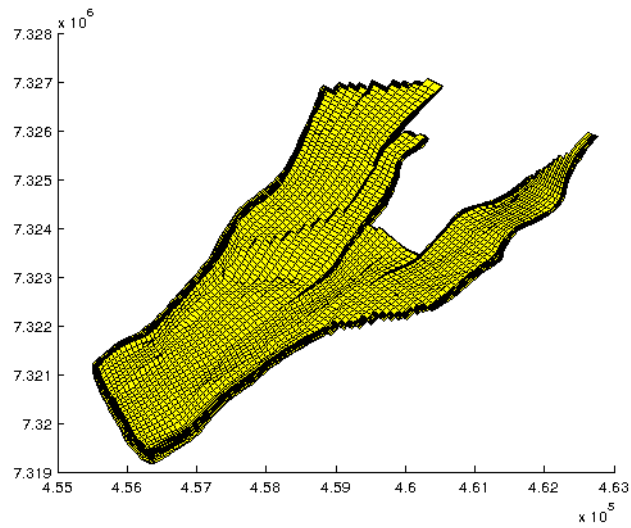
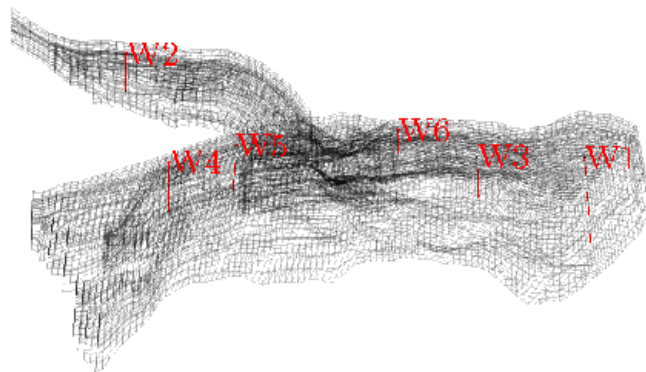**Figure 5.12:** *The real field model.*



**Figure 5.13:** *Model with wells.*

We want to compare the number of cycles for the hybrid mimetic method and the mimetic method. We will consider two different cases concerning the permeability. The first case will have a homogeneous isotropic permeability of **K** = diag$(1, 1, 1)$ Darcy.

The second case will have a heterogeneous anisotropic permeability which is the estimated permeability of the respective reservoir. This permeability is very layered, i.e., we have layers where the permeability in this layer of the reservoir can be considered homogeneous.

We will for the two cases consider the number of cycles in the flux field, i.e., the cycles in the flux-matrix. We have chosen a tolerance of tol $= |f|_{max} \cdot 10^{-13}$ which means that all the fluxes that have an absolute value smaller than the tolerance is set to 0. This is done as we do not want to consider cycles caused by very small fluxes as we can neglect such fluxes.

## 5.8.1   Homogenous isotropic permeability

We will now consider the case where we have homogeneous isotropic permeability, $\mathbf{K} = \text{diag}(1,1,1)$.

The pressure solutions obtained by TPFA, the mimetic method using the inner product `ip_simple` and the hybrid mimetic method are shown in Figure 5.14. We see that the three methods give quite similar solutions. We cannot compare these solutions to any analytic answer.

Table 5.13 shows R, the ratio of cells in cycles, N, the number of cycles and $n_{max}$, the size of the largest cycle for the mimetic and the hybrid mimetic method. The difference in R is not extremely large, but we find a difference, and the hybrid mimetic method has more cells in cycles and more cycles in total than the mimetic method. This is in fact a surprising result since we expected that the hybrid method would have fewer cycles than the full method since it uses TPFA in the vertical direction.

**Table 5.13:** *Results concerning cycles for the flux field with homogeneous isotropic permeability. R is ratio of cells in cycles, N is the number of cycles and $n_{max}$ is the size of the largest cycle.*

| Method | R | N | $n_{max}$ |
|---|---|---|---|
| Hybrid mimetic | 0.1110 | 279 | 215 |
| Mimetic | 0.0693 | 218 | 242 |

We have in Figure 5.15 plotted the flux-matrix and the red blocks represent the cycles. We can see that the hybrid mimetic method have more cycles than the mimetic method when the permeability is homogeneous and isotropic. Note that the blocks are drawn ten times larger than the cycles actually are in order to see them better, i.e., the length of each side of the square is ten times the length of the cycle.

## 5.8.2   Heterogeneous anisotropic permeability

We now consider the field with a heterogeneous anisotropic permeability. This is the estimated permeability for the actual reservoir and the permeability in the $xy$-direction
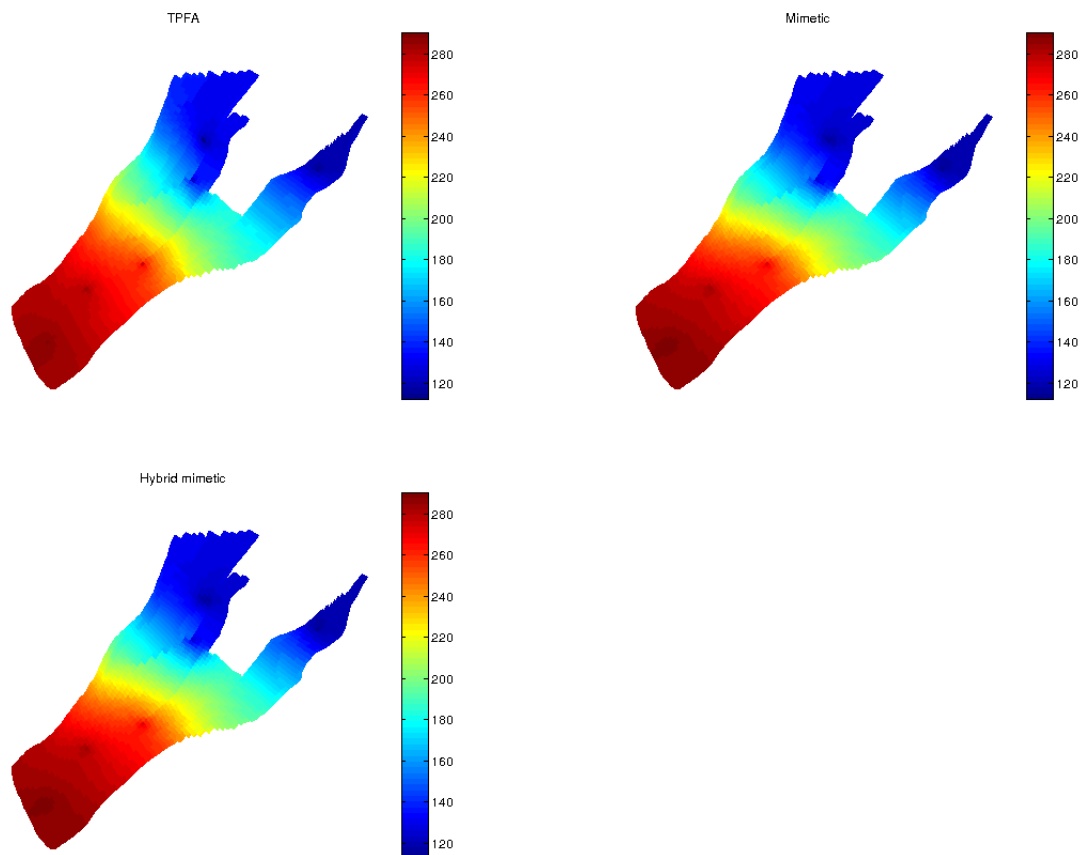
**Figure 5.14:** *Pressure solution. TPFA on the top left, mimetic on the top right and the hybrid mimetic on the bottom.*

is larger than in the *z*-direction, and the permeability varies through the different layers. The pressure solution for this case looks similar to the case above, and we therefore do not show the plot.

Table 5.14 shows C, N and $n_{max}$ for the mimetic hybrid method and the mimetic method using `ip_simple`. As for the previous case we have set tol $= |f|_{max} \cdot 10^{-13}$.

**Table 5.14:** *Results concerning cycles for the flux field with heterogeneous anisotropic permeability. R is ratio of cells in cycles, N is the number of cycles and $n_{max}$ is the size of the largest cycle.*

| Method | R | N | $n_{max}$ |
|---|---|---|---|
| Hybrid mimetic | 0.0592 | 359 | 324 |
| Mimetic | 0.1445 | 528 | 648 |

The mimetic method results in more cycles in the flux field than the hybrid method, and R is almost three times larger for the mimetic method than the hybrid mimetic method. The hybrid mimetic method has fewer cycles now, when the permeability is anisotropic than when the permeability was isotropic. For this case the mimetic
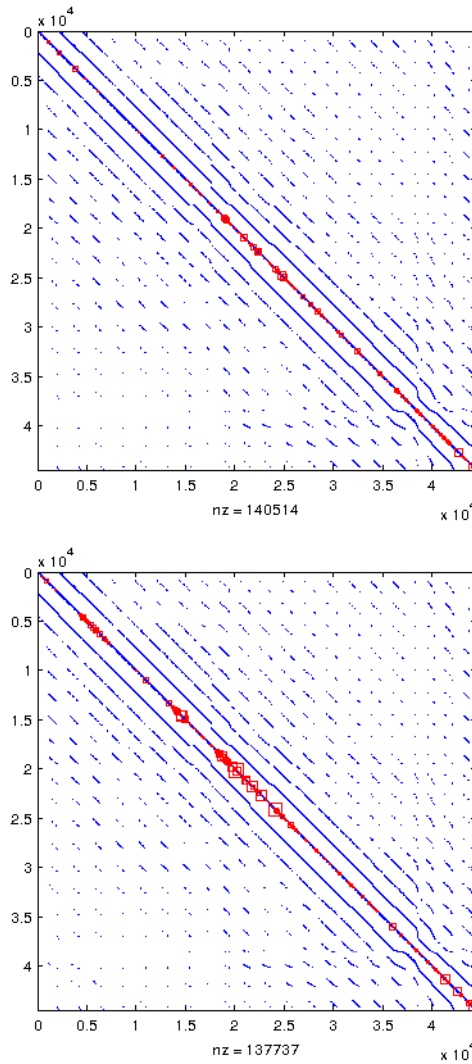
**Figure 5.15:** *Homogeneous isotropic permeability: The flux-matrices with cycles, the mimetic on top and the hybrid mimetic on the bottom.*

method has more cycles than the hybrid mimetic method, and this was what we expected.

We have visualised the cycles in Figure 5.16. Note that here, as in Section 5.8.1, the red blocks are drawn 10 times as large as the cycles are.

We want to check if the tolerance tol $= |f|_{max} \cdot 10^{-13}$ is too strict, and hence we will check the number of cycles if we instead set the tolerance to: tol $= |f|_{max} \cdot 10^{-9}$, $|f|_{max} \cdot 10^{-6}$ and $|f|_{max} \cdot 10^{-3}$.

We have also plotted the matrices and the cycles for the different tolerances in Figure 5.17, Figure 5.18 and Figure 5.19. The plots to the left is when the mimetic method is used, and the plot to the right is when the hybrid mimetic method is used.

By comparing Table 5.15 and Table 5.16 to Table 5.14, we note that by choosing the tolerance to be $|f|_{max} \cdot 10^{-9}$ or $|f|_{max} \cdot 10^{-6}$ gives answers which are quite similar to a
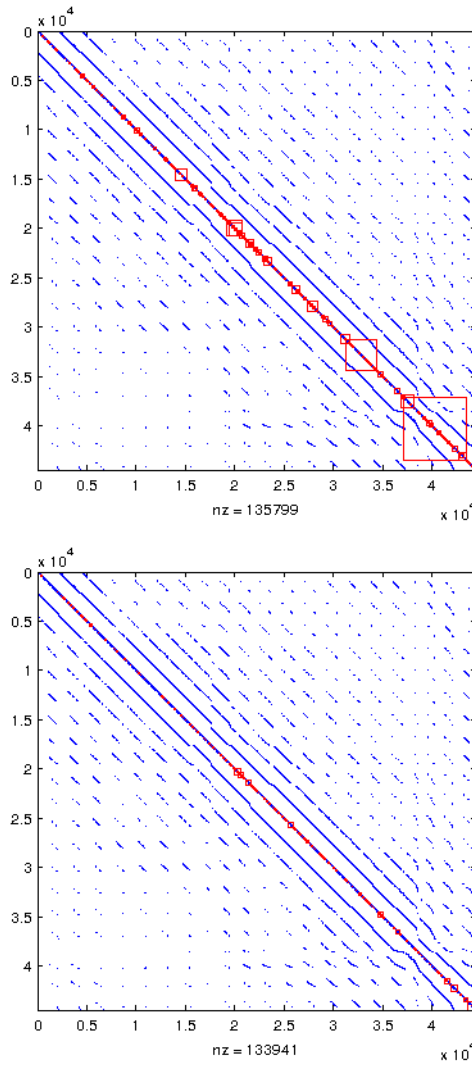
**Figure 5.16:** *Heterogeneous anisotropic permeability: The flux-matrix with cycles the mimetic on top and the hybrid mimetic bottom*

**Table 5.15:** *Setting different tolerances for the hybrid mimetic method. R is ratio of cells in cycles, N is the number of cycles and $n_{max}$ is the size of the largest cycle.*

| Tolerance | R | N | $n_{max}$ |
|---|---|---|---|
| $|f|_{max} \cdot 10^{-9}$ | 0.0589 | 359 | 324 |
| $|f|_{max} \cdot 10^{-6}$ | 0.0533 | 337 | 323 |
| $|f|_{max} \cdot 10^{-3}$ | 0.0015 | 15 | 10 |

tolerance of $|f|_{max} \cdot 10^{-13}$. If the tolerance is set to $|f|_{max} \cdot 10^{-3}$ we have few and small cycles. However, we assume that this tolerance is too high and when choosing this tolerance we exclude some important flux values. We can say that the tolerance of $|f|_{max} \cdot 10^{-13}$ is not too strict since choosing a somewhat higher tolerance does not result in a too different answer.

As explained in Section 3.2 it is of interest to consider the number of times when

**Table 5.16:** *Setting different tolerances for the mimetic method. R is ratio of cells in cycles, N is the number of cycles and $n_{max}$ is the size of the largest cycle.*

| Tolerance | R | N | $n_{max}$ |
|---|---|---|---|
| $\|f\|_{max} \cdot 10^{-9}$ | 0.1439 | 528 | 648 |
| $\|f\|_{max} \cdot 10^{-6}$ | 0.1330 | 511 | 638 |
| $\|f\|_{max} \cdot 10^{-3}$ | 0.0134 | 67 | 58 |

$u(n_1) \geq u(n_2)$, but the flux from cell 1 to cell 2, $f_{1,2} \leq 0$.

**Table 5.17:** *The number of times when $f_{1,2} \leq 0$ while $u(n_1) \geq u(n_2)$ for the different methods.*

| Method | $f_{1,2} \leq 0$ | Ratio |
|---|---|---|
| Hybrid mimetic | 1888 | 0.0425 |
| Mimetic | 10011 | 0.2254 |

From Table 5.17 we see that there is a large difference between the number of times this happens for the mimetic method and the hybrid mimetic method. The hybrid mimetic method uses TPFA for two half-faces for each cell, and for a cell with six faces the mimetic part of the hybrid method is performed on $\frac{2}{3}$ of the cell, and thus we have already neglected those faces concerning the direction of the flux compared to the pressure drop. From Table 5.17 we see that this occurs five times more for the mimetic method than for the hybrid mimetic method. This may be caused by the fact that if we first have one case where this happens this will effect the other calculated fluxes.

We have considered a real field model where the grid cells have a larger extent in the plane than in the vertical direction. The permeability is anisotropic where the permeability in the $z$-direction is smaller than in the plane and the permeability is layered, i.e., we have layers where the permeability is almost constant. For this grid we see that the results obtained by the hybrid mimetic method contains fewer cycles in the flux field than the mimetic method. The number of cells in cycles is almost three times higher for the mimetic method than for the hybrid mimetic method. The number of times that $u(n_1) \geq u(n_2)$, and the flux from cell 1 to cell 2, $f_{1,2} \leq 0$ is five times higher for the mimetic method compared to the hybrid method. Using the hybrid mimetic method applying the mimetic method in the plane and TPFA in the vertical direction instead of using the mimetic method in the entire domain result in a reduction of cycles for this case.

In this chapter we have presented the results from testing five different discretisation methods on various cases. We have shown that the hybrid methods are exact when we have linear flow. We have also shown that by using hybrid methods applying TPFA in the vertical direction we reduce the number of nonphysical cycles for special cases.
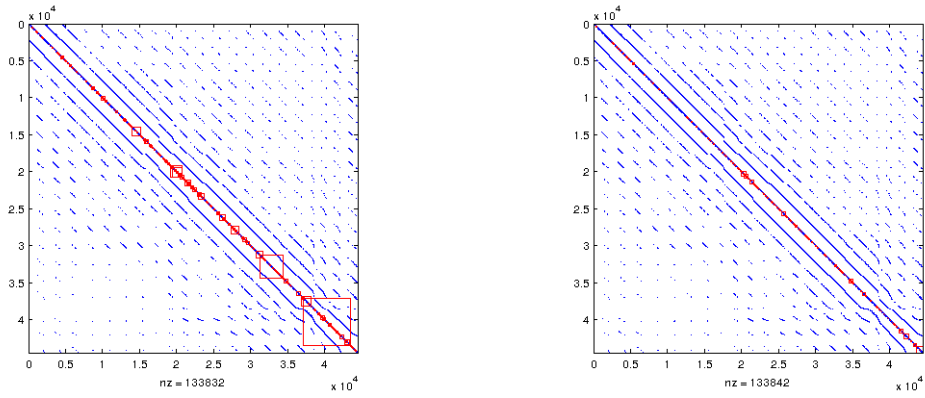
**Figure 5.17:** *Tolerance = $|f|_{max} \cdot 10^{-9}$ for the mimetic method to the left, and the hybrid mimetic method to the right.*
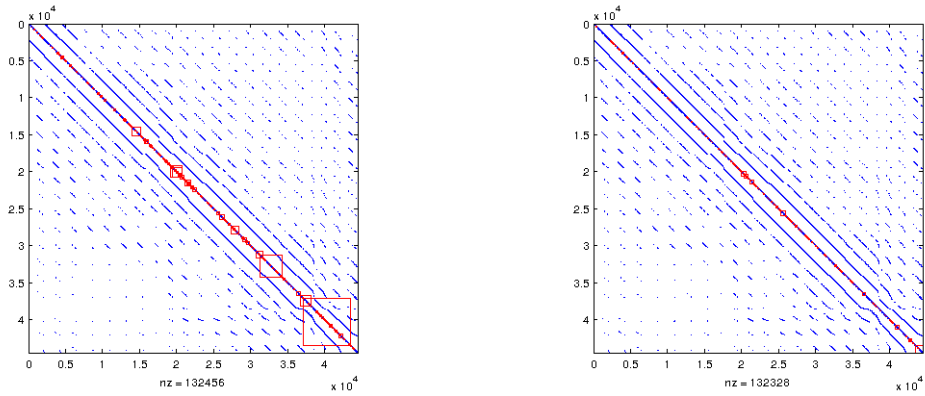


**Figure 5.18:** *Tolerance = $|f|_{max} \cdot 10^{-6}$ for the mimetic method to the left, and the hybrid mimetic method to the right.*
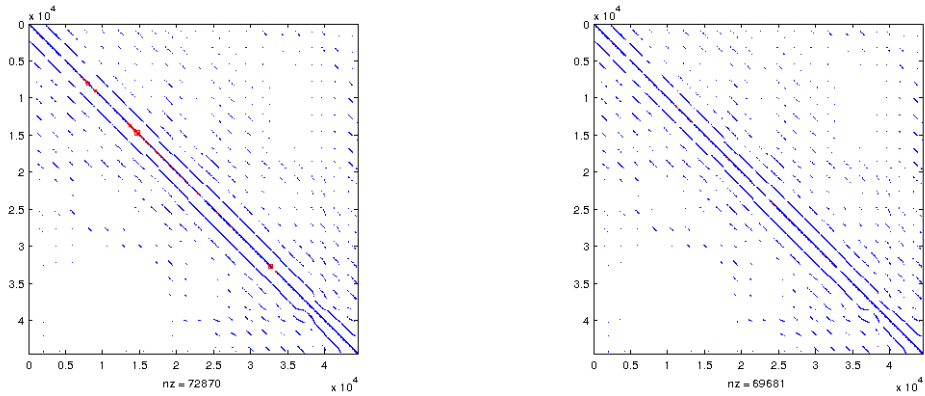


**Figure 5.19:** *Tolerance = $|f|_{max} \cdot 10^{-3}$ for the mimetic method to the left, and the hybrid mimetic method to the right.*

# Chapter 6

# Discussion, conclusion and further work

The goal of this thesis was to develop a method using TPFA in the vertical direction and a consistent method in the plane. The motivation for doing this was to obtain a method which is more consistent than TPFA and results in fewer cycles in the flux field compared to using the consistent method in the entire domain.

We have presented the theoretical background for TPFA which is the most common method used within reservoir simulations. We have also provided the theoretical background for the consistent mimetic discretisation methods and MPFA. We have explained how the loss of monotonicity may result in nonphysical cycles in the flux field and why this should be avoided. Two hybrid methods were developed, the first applies TPFA and a mimetic method, and the second applies TPFA and MPFA. We have tested the five methods on various cases and compared the results in relation to accuracy and cycles.

## 6.1 Discussion

In Sections 5.1-5.3 we noted that the hybrid methods gave the exact answers in situations with linear flow, and where the top an bottom faces were aligned with the $xy$-plane. TPFA provides the exact answer when we have linear flow and the grid is **K**-orthogonal. However, if the grid is not **K**-orthogonal errors occur. This was the situation for a grid where the cells were triangular in the plane, and for a pebi grid where the top and bottom faces were parallel. For these cases, both hybrid methods provided the correct answer, and the hybrid methods are thus consistent on grids that are not **K**-orthogonal, but with parallel top and bottom faces in the $xy$-plane. Results for a one-layered real field model that was flattened, i.e., the top and bottom faces were parallel also showed that the hybrid methods were more consistent than TPFA.

We also compared the results if we had a grid with an increasing angle between the grid and the $xy$-plane and if the anisotropic rate $\frac{\text{permX}}{\text{permZ}}$ increased, note that permY =

permX. The results showed that the hybrid methods did not include any cycles for any of the cases, but the consistent methods had cycles if the anisotropic rate was very large. Another important finding was that for grids with very skew pillars, but the ratio $Dx/Dz$ was large enough, the hybrid methods provided answers with high degree of accuracy. However, concerning the specific case presented, TPFA also gave answers with high degrees of accuracy, and it is therefore as expected that the hybrid methods gave satisfying answers.

For the large pebi grid explained in Section 5.7 we found that the answers provided by the hybrid methods contained no cycles in the flux field even if we had anisotropic permeability. The results provided by the full consistent methods contained cycles, but only a few. This may result from the fact that this case had a close to linear flow, and the grid cells were quite regular and only limitedly skew and cycles seldom occur in such cases.

We also considered a real field model, but here we only considered the mimetic method and the hybrid mimetic method. A surprising result was that for homogeneous isotropic permeability, the mimetic method had fewer cycles than the hybrid method. We believed at the outset that that the hybrid mimetic method would never contain more cycles than the mimetic method since this method applies the mimetic method in the plane and TPFA in the vertical direction and TPFA never results in cycles. When a layered heterogeneous anisotropic permeability was considered, we found that the hybrid mimetic method resulted in fewer cycles than the mimetic method. We found more cells in cycles, more cycles and the largest cycle was larger for the mimetic method than the hybrid mimetic method.

## 6.2   Conclusion

Based on the results from this thesis, we can conclude that the hybrid methods are more accurate than TPFA. The hybrid methods are especially well suited for cases where the grid is not **K**-orthogonal, the top and bottom faces are approximately parallel and when the extent of the $x$- and $y$-direction are large compared to the $z$-direction.

We observed concerning cycles that the hybrid methods gives the largest reduction in cycles if we have grids with very skew vertical pillars and the anisotropic permeability rate is high. If in addition the anisotropic permeability is constant within layers we get good results when the hybrid methods are used. The results were not as distinct as we had expected at the outset, but we note a difference in favor of the hybrid methods when concerning cycles.

## 6.3   Further work

The implementation of the hybrid methods has not been done in the most optimal way in this thesis. In further developing of these methods, they should be implemented

in a less time consuming way. It should be important and interesting to explore the time aspect of the hybrid methods since they for some cases are as accurate as the full methods, but less time consuming if they are implemented correctly. In addition, as explained in Section 4.2, we should have implemented the hybrid MPFA method in a better way, even if we do not consider the time aspect. Therefore, it should be important to modify the hybrid MPFA function by projecting the faces that are not top or bottom down to the $xy$-plane and apply the two-dimensional MPFA here and TPFA in the vertical direction.

It can also be of interest to further investigate if it is possible to develop hybrid methods based on other consistent methods than the mimetic method and MPFA leading to better results in relation to cycles in the flux field.

# Bibliography

[1] T. Gimse, J. E. Aarnes, and K.-A. Lie, "An introduction to the numerics of flow in porous media using matlab," in *Geometrical Modeling, Numerical Simulation, and Optimization*, G. Hasle, K.-A. L. Lie, and E. Quak, Eds. Springer Verlag, 2007, pp. 265–306.

[2] J. Kleppe, *Lecture notes in TPG4160 Reservoir Simulation*, Norwegian University of Science and Technology, Department of Petroleum Engineering and Applied Geophysics. [Online]. Available: http://www.ipt.ntnu.no/~kleppe/TPG4160/index.html

[3] I. Aavatsmark, *Bevarelsesmetoder for elliptiske differensialligninger*. Universitetet i Bergen, Anvendt og beregningsorientert matematikk, 2007. [Online]. Available: \url{folk.uib.no/fciia/elliptisk.pdf}

[4] H. K. Hvidevold, "Monotonicity conditions for discretization of parabolic conservation laws," Master of Science Thesis in Applied Mathematics, Department of Mathematics, University of Bergen, 2009.

[5] K. Lie, S. Krogstad, I. Ligaarden, J. Natvig, H. Nilsen, and B. Skaflestad, "Open-source matlab implementation of consistent discretisations on complex grids," *Computational Geosciences*, vol. 16, no. 2, pp. 297–322, 2012.

[6] I. Aavatsmark, "An introduction to multipoint flux approximations for quadrilateral grids," *Computational Geosciences*, vol. 6, no. 3, pp. 405–432, 2002.

[7] K. Lipnikov, M. Shashkov, and I. Yotov, "Local flux mimetic finite difference methods," *Numerische Mathematik*, vol. 112, no. 1, pp. 115–152, 2009.

[8] J. Hyman, J. Morel, M. Shashkov, and S. Steinberg, "Mimetic finite difference methods for diffusion equations," *Computational Geosciences*, no. 6, pp. 333–352, 2002.

[9] R. Juanes, J. Kim, S. Matringe, and L. Thomas, "Implementation and application of a hybrid multipoint flux approximation for reservoir simulation on corner-point grids." Society of Petroleum Engineers, 2005. [Online]. Available: http://www.onepetro.org/mslib/servlet/onepetropreview?id=SPE-95928-MS

[10] "Mrst - matlab reservoir simulation toolobox." [Online]. Available: \http://www.sintef.no/Projectweb/MRST/2011b

[11] F. Brezzi, K. Lipnikov, and V. Simoncini, "A family of mimetic finite difference methods on polygonal and polyhedral meshes," *Mathematical Models and Methods in Applied Sciences*, vol. 15, no. 10, pp. 1533–1551, 2005.

[12] E. Keilegavlen and I. Aavatsmark, "Monotonicity for mpfa methods on triangular grids," *Computational Geosciences*, vol. 15, no. 1, pp. 3–16, 2011.

[13] L. C. Evans, *Partial Differential Equations*, 2nd ed.   American Mathematical Society, 2010, vol. 19.

[14] K.-A. Lie, J. R. Natvig, and H. M. Nilsen, "Discussion of dynamics and operator splitting techniques for two-phase flow with gravity," *International journal of numerical analysis and modeling*, vol. 9, no. 3, pp. 684–700, 2012.

[15] J. R. Natvig and K.-A. Lie, "Fast computation of multiphase flow in porous media by implicit discontinuous galerkin schemes with optimal ordering of elements," *Computational Physics*, vol. 227, pp. 10 108–10 124, 2008.

[16] T. C. Cormen, C. E. Leiserson, R. L. Rivest, and C. Stein, *Introduction to algorithms*, 3rd ed.   The MIT Press, Massachusetts Institute of Technology, 2009.

[17] K.-A. Lie, *Simulating flow in porous media using the Matlab Reservoir Simulation Toolbox*, 2011, book manuscript, in preparation.